JGR Oceans

RESEARCH ARTICLE

10.1029/2020JC016814

Key Points:

- Sea-ice meltwater controls the buoyancy of the mixed layer during early summer
- Mixed layer eddies grow from mesoscale meltwater lateral gradients but are confined to the surface boundary layer
- Observations suggest that mixed layer variability at submesoscales is dominated by wind-front interactions

Supporting Information:

Supporting Information may be found in the online version of this article.

Correspondence to:

I. Giddy,
isgiddy@gmail.com

Citation:

Giddy, I., Swart, S., du Plessis, M., Thompson, A. F., & Nicholson, S.-A. (2021). Stirring of sea-ice meltwater enhances submesoscale fronts in the Southern Ocean. *Journal of Geophysical Research: Oceans*, *126*, e2020JC016814. https://doi.org/10.1029/2020JC016814

Received 22 SEP 2020
Accepted 2 MAR 2021

Stirring of Sea-Ice Meltwater Enhances Submesoscale Fronts in the Southern Ocean

I. Giddy[1,2,3], S. Swart[1,2], M. du Plessis[2,3], A. F. Thompson[4], and S.-A. Nicholson[3]

[1]Department of Oceanography, University of Cape Town, Rondebosch, South Africa, [2]Department of Marine Sciences, University of Gothenburg, Gothenburg, Sweden, [3]Southern Ocean Carbon-Climate Observatory, CSIR, Cape Town, South Africa, [4]Environmental Science and Engineering, California Institute of Technology, Pasadena, CA, USA

Abstract In the sea-ice-impacted Southern Ocean, the spring sea-ice melt and its impact on physical processes set the rate of surface water mass modification. These modified waters will eventually subduct near the polar front and enter the global overturning circulation. Submesoscale processes modulate the stratification of the mixed layer (ML) and ML properties. Sparse observations in polar regions mean that the role of submesoscale motions in the exchange of properties across the base of the ML is not well understood. The goal of this study is to determine the interplay between sea-ice melt, surface boundary layer forcing, and submesoscale flows in setting properties of the surface ML in the Antarctic marginal ice zone. High-resolution observations suggest that fine-scale lateral fronts arise from either/both mesoscale and submesoscale stirring of sea-ice meltwater anomalies. The strong salinity-driven stratification at the base of the ML confines these fronts to the upper ocean, limiting submesoscale vertical fluxes across the ML base. This strong stratification prevents the local subduction of modified waters by submesoscale flows, suggesting that the subduction site that links to the global overturning circulation does not correspond with the location of sea-ice melt. However, surface-enhanced fronts increase the potential for Ekman-driven cross-frontal flow to modulate the stability of the ML and ML properties. The parameterization of submesoscale processes in coupled-climate models, particularly those contributing to the Ekman buoyancy flux, may improve the representation of ML heat and freshwater transport in the ice-impacted Southern Ocean during summer.

Plain Language Summary Sea-ice melt around Antarctica is an annual event in which the state of the surface ocean is transformed, during which over 15 trillion liters of freshwater enter the upper ocean. This fresh layer separates the upper ocean from the deep ocean and suppresses the exchange of heat and gases—like carbon dioxide—between the deep ocean and the atmosphere, with important implications for the climate system. Using state-of-the-art autonomous underwater gliders, we observed key physical properties of the surface ocean following the melt of sea-ice. The presence of fine-scale fronts (sharp changes in density), of less than 10 km at horizontal scales, revealed that sea-ice melt not only stabilizes the upper ocean, but also provides additional energy for small eddies and filaments to form. While the eddies are unable to extend deeper than the fresher surface layer, they enhance the ocean response to winds. These findings may contribute to the improvement of global climate models and our understanding of how the ocean will react to changes in sea-ice under a warmer climate.

1. Introduction

Around Antarctica, sea-ice forms a relatively thin (~1 m) insulative layer over the ocean's surface, covering an area of ~19 million km^2 (roughly equivalent in size to the Antarctic continent itself) and retreating to an area of ~3 million km^2 in summer (Parkinson, 2014). The expansion and contraction of sea-ice is important for Southern Ocean heat uptake since it modulates the transfer of heat between the atmosphere and deep waters through its influence on the salinity and density of the surface waters (Bitz et al., 2006; Kirkman & Bitz, 2011). However, climate models continue to diverge in their representation of heat and carbon exchange in the Southern Ocean (Frölicher et al., 2015). With the paucity of observations south of 50°S (Newman et al., 2019; Swart et al., 2019), some of the model uncertainties can likely be attributed to misrepresented atmosphere-ocean processes associated with the sea-ice-impacted Southern Ocean (Chemke & Polvani, 2020).

The seasonal melt of Antarctic sea-ice is the primary source of freshwater in the Southern Ocean south of 50°S (Abernathey et al., 2016). When the melting of sea-ice occurs in the spring, freshwater (more than 15 trillion liters) is reintroduced into the surface waters and advected by Ekman processes (Speer et al., 2000) northwards. This phenomenon is associated with net freshening and lightening of the mixed layer (ML) (Pellichero et al., 2017). Through the resultant impact on water mass transformation (Abernathey et al., 2016), the ice-impacted ML acts as a conduit between sea-ice dynamics and the global ocean circulation (e.g., Haumann et al., 2016; Pellichero et al., 2018).

At the northern edge of the sea-ice, a dynamic band of low concentration sea-ice defines the marginal ice zone (MIZ), separating the open ocean from the ice pack. One-dimensional mixing processes associated with local sea-ice melt and vertical mixing have been shown to dominate upper ocean physics in MIZs (Dewey et al., 2017; Smith et al., 2018). However, it has been demonstrated by theory and models that submesoscale flows in MIZs interact with horizontal gradients in density to modify ML structure (Horvat et al., 2016; Lu et al., 2015; Manucharyan & Thompson, 2017), and by observations in the Arctic (Brenner et al., 2020; Koenig et al., 2020; Timmermans & Winsor, 2013) and more recently in the Antarctic (e.g., Biddle & Swart, 2020; Swart et al., 2020).

ML baroclinic instabilities (MLIs, Fox-Kemper et al., 2008), a class of submesoscale flows, are characterized dynamically by order one Richardson and Rossby numbers (McWilliams, 2016; Thomas et al., 2008). MLIs give rise to mixed layer eddies (MLEs), which can increase surface stratification through an eddy overturning and induce large vertical velocities and fluxes. In this way, surface stratification is influenced both diabatically through heat gain and loss to the atmosphere, and adiabatically, through dynamical restratification by frontal slumping. While a range of submesoscale flows can impact surface boundary layer variability, MLEs, associated with baroclinic instabilities, are ubiquitous in the surface ocean.

MLI has the potential to structure the upper ocean in sea-ice-impacted regions. A combination of simulations and observations by Horvat et al. (2016) and Lu et al. (2015) show MLI can be formed from freshwater fronts by melted sea-ice and result in the horizontal mixing of heat, enhancing the melt of nearby ice floes. Similarly, Manucharyan and Thompson (2017) model MLI which feed off existing frontal structures in a MIZ. The submesoscale structuring of fronts and filaments leads to intermittent fluxes of heat and sea-ice which can contribute to the structuring of the upper ocean in MIZs. MLEs, which grow from the MLI, may contribute to the flux of underlying warmer water to the surface. Adding a layer of complexity, von Appen et al. (2018) propose that subduction associated with baroclinic instabilities and ML fronts is enhanced due to increased mixing from cabbeling—when two water masses of the same density mix and the resultant water mass is denser. MLEs tend to give rise to increased stratification; however, Brenner et al. (2020) could not conclusively show that eddies formed from baroclinic instabilities were a leading factor in setting the ML stratification. Their study suggests that MLEs may not be sufficiently strong in MIZs to impact upper-ocean stratification. The results from ice-covered (Timmermans et al., 2012) and ice-free (Timmermans & Winsor, 2013) Arctic MIZ observational campaigns provide evidence for submesoscale restratification, albeit with potential density spectral slopes steeper (k^{-3}) than the upper ocean boundary layer in the open ocean mid-latitudes (k^{-2}), suggesting that different physical mechanisms are controlling the horizontal structure of the upper ocean compared to mid-latitudes. In the Antarctic, evidence of active MLI has been observed (Biddle & Swart, 2020), even under suppressed surface forcing (reduced wind and solar heat loss from sea-ice cover), emphasizing the role of sea-ice fronts in the production of submesoscale instabilities. While it has been shown that MLI is actively structuring the ML in MIZs—through restratification or lateral and vertical mixing—it remains uncertain in observations whether MLI is strong enough to result in significant vertical fluxes across the base of the ML in the strongly stratified MIZs.

Observations of wind-front interactions in ice-free MIZs yield contrasting results between the studies. Under winter conditions near the Arctic MIZ, Koenig et al. (2020) provide evidence of sustained turbulence by forced symmetric instabilities associated with downfront winds and heat loss from the surface layer, which extract potential vorticity from the water column at submesoscale fronts. Conversely, Brenner et al. (2020) found that upfront winds lead to frontogenesis on time scales shorter than Ekman dynamics. The Antarctic MIZ differs from the Arctic in that the Antarctic sea-ice sector experiences strong, event-scale storms (Patoux et al., 2009; Vichi et al., 2019). Swart et al. (2020) suggest that in the stormy conditions of the Antarctic MIZ, wind forced thermohaline shear dispersion, in combination with slumping by MLEs, act to reduce the strength of freshwater surface layer fronts. When the winds subside, fronts are able to reform by the stirring of the fresher surface layer by mesoscale eddies and therefore persist well into the summer.

Submesoscale motions and instabilities are seasonal across the world's oceans, with stronger flows under winter/low ML stratification conditions (Callies et al., 2015). In the Antarctic MIZ during summer, solar heating and freshwater input from bulk sea-ice melt both act to stratify the surface layer (Swart et al., 2020), similar to other freshwater-driven systems (e.g., Gulf of Mexico; Luo et al., 2016). However, while the freshwater influx stratifies the ML, the dispersing freshwater, originating from sea-ice melt, also introduces mesoscale fronts from which submesoscale instabilities can form. The dynamic nature of the Southern Ocean surface layer, influenced by strong winds and passing storms, maintains stratification weaker than otherwise. This sets up a unique interplay between submesoscale ML fronts, stratifying 1D ocean-atmosphere buoyancy fluxes and destratifying mechanical mixing by winds. Dissecting these interactions and their seasonal evolution is the topic of this study.

The preceding research suggests that the properties of the surface layer in polar MIZs are not driven purely by one-dimensional processes. Here, we hypothesize that the persistence of submesoscale activity in the ice-free Antarctic MIZ is associated with northwards advecting freshwater from sea-ice melt. We use high resolution in situ data in combination with satellite and reanalysis products to interrogate the evolution of the ML in the Antarctic MIZ, from immediately after sea-ice melt to the end of summer.

2. Data and Methods

2.1. Study Region

The Robotic Observations and Modeling of the Marginal Ice Zone (ROAM-MIZ) project (2019–2023) involves a field campaign set in the Antarctic MIZ, south of the southern boundary of the Antarctic circumpolar current (ACC) (Figure 1a), with a key objective of characterizing the role of submesoscale flows on stratification, air-sea fluxes and mixed-layer-interior exchange in the sea-ice-impacted Southern Ocean. Satellite color imagery (from 7 January, at a nominal spatial resolution of ∼0.3 km, Figure 1b) reveal surface chlorophyll concentrations that suggest the presence of both mesoscale and submesoscale variability. The study region is covered entirely by sea-ice during the winter (Figure 1d).

The maximum and minimum sea-ice extent for the 2018–2019 season occurred on September 3, 2018 and February 23, 2019, respectively (computed as the maximum integral of pixels with a sea-ice concentration >0.15 from AMSR2; Figures 1a and 1d). The surface ocean is impacted by ocean-atmosphere buoyancy fluxes (here confined to surface heating defined as the sum of shortwave, longwave, latent and sensible heat, plus evaporation-precipitation (E-P); refer to Section 2.4 for a more detailed explanation of the data used). At the ROAM-MIZ site, ocean-atmosphere buoyancy fluxes peak on 25 December at 256 W m^{-2}, largely attributable to incoming solar heat (Figures 2a and 2b). Precipitation events occurred throughout the summer season (Figure 2b). The mean wind stress is 0.09 ± 0.08 N m^{-2} with three wind events (storms) reaching 0.4–0.6 N m^{-2} (Figure 2c). Wind direction was variable, but predominantly westerly.

2.2. Seaglider Mission and Data Processing

A Seaglider was deployed at 60°S, 0°E, 445 km south of the southern boundary of the ACC, estimated using the criteria of Swart et al. (2010), based on contours of SSH (Figure 1b). The deployment commenced in early summer (December 14, 2018), just four days after the melt of sea-ice when the surface heat flux into the ocean was almost at its maximum (Figure 1d), and continued for 102 days, until 26 March. The Seaglider was piloted in a "bow-tie" sampling pattern completing repeat transects of approximately 20 km in length. The bow-tie sampling strategy was adopted as there is no preferred orientation of lateral gradients at submesoscales. Thus the bow-tie pattern provides a statistical representation of the lateral gradients in the region (see Section 2.5). To assess the background mesoscale field, at the start and middle of the mission, two north-south mesoscale transects (185 and 120 km, respectively) were completed. In total, the Seaglider covered a distance of 2,074 km, collecting 974 profiles, 1,000 m in depth. Noting that Seagliders sample in both time and space, for the analysis, we interpret the data in an Eulerian sense, similar to the approach used by du Plessis et al. (2019).

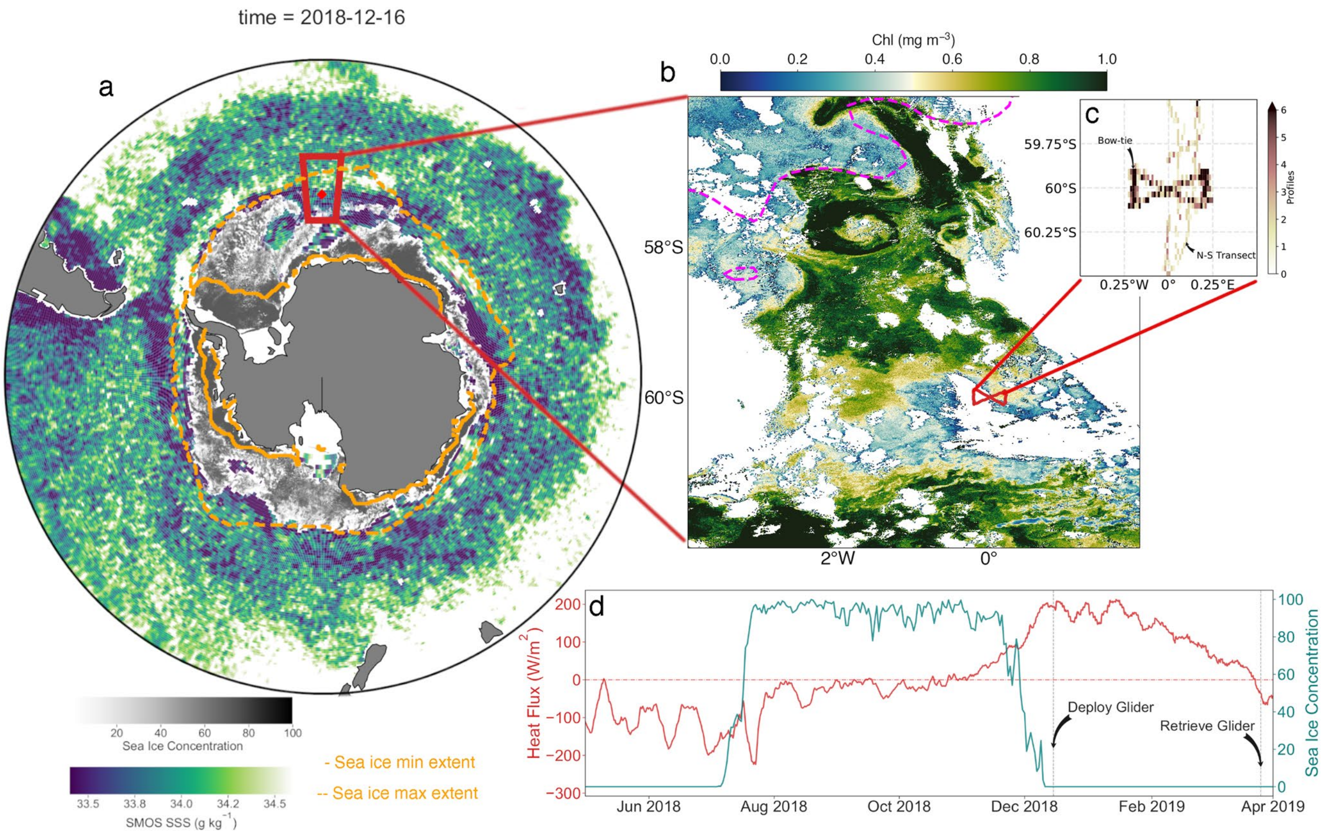

Figure 1. (a) Regional view of the ROAM-MIZ study site, showing SMOS salinity on December 16, 2018, and the sea-ice concentration at the time of deployment (December 14, 2018). Maximum and minimum sea-ice extent for the year 2018–2019 are contoured in dotted and solid orange lines, respectively. (b) A snapshot of Sentinal-3A OCLI Chlorophyll Ocean Color in cloud-free conditions on January 6, 2020, during the deployment. The southern boundary of the ACC is demarcated by the dashed magenta line. The deployment is marked by the red bow-tie, reflecting the sampling pattern that was maintained for the duration of the deployment. (c) Heat map showing the spatial distribution of profiles captured by the Seaglider. (d) Annual time series of net downward heat flux and sea-ice concentration at 60°S, 0°E. Zero heat flux is marked with a dash-dot red line. The time of deployment and retrieval of the Seaglider is indicated by the black arrows. SMOS, Soil Moisture Ocean Salinity.

The Seaglider sampled temperature and conductivity (salinity) nominally at 0.2 Hz, equating to a vertical resolution of 0.2–1.5 m, with an average resolution of 0.5 m in the upper 400 m. The Seaglider data were prepared for analysis using GliderTools (Gregor et al., 2019). Salinity and temperature were converted to absolute salinity and conservative temperature, respectively, using the Gibbs Seawater toolbox (McDougall & Barker, 2011). Finally, the Seaglider conductivity and temperature data were corrected against the calibrated shipborne data from conductivity-temperature-depth (CTD) casts at the deployment and retrieval of the Seaglider (as per Swart et al., 2015). The mixed layer depth (MLD) is calculated from the Seaglider data using the density difference criteria of 0.03 kg m^{-3} from a reference depth of 10 m (de Boyer Montgut et al., 2004).

2.3. Thermal Lag Correction of Salinity

Small errors in profile-to-profile temperature and salinity estimates can artificially enhance estimates of lateral buoyancy gradients. The accurate estimation of submesoscale fluxes, which are a function of lateral buoyancy gradients, demands minimizing instrumental error.

Salinity is inferred from measured conductivity and temperature. A temperature sensor measures seawater temperature outside of the conductivity cell, while a conductivity sensor measures seawater conductivity inside of the conductivity cell. This spatiotemporal mismatch introduces an offset in the temperature of the water that the conductivity sensor actually measures, resulting in thermal lag that needs to be corrected to

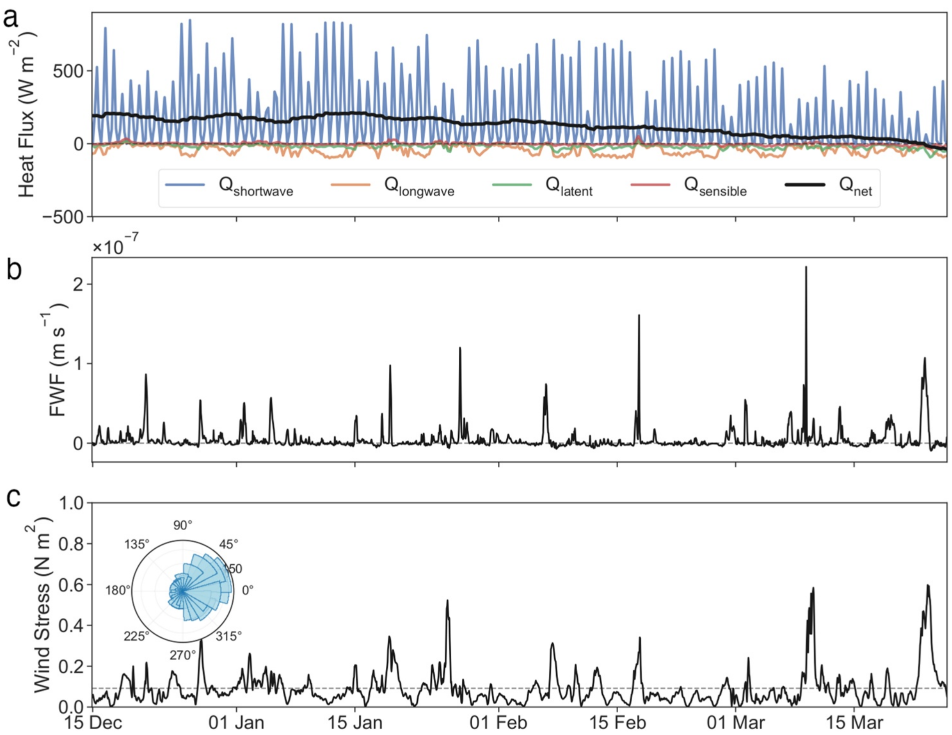

Figure 2. Summer time series of surface forcing from ERA5 reanalysis at the ROAM-MIZ site between December 2018 and March 2019. (a) Surface heat flux decomposed into its components: shortwave, longwave, sensible, and latent heat flux with the sum of components, the net surface heat flux plotted in black. A running mean of 24 h is applied to the net surface heat flux, (b) surface freshwater flux (E–P), and (c) wind stress with the distribution of the wind direction inset. The average wind stress is marked with a gray dashed line.

obtain accurate salinity measurements. The presence of thermal lag in data results in errors in salinity and density, especially at the thermocline where there are sharp gradients in temperature and salinity.

In the case of unpumped CTDs, the vehicle propulsion is what induces flow through the sensor. Thermal-lag effects change as the speed of the vehicle fluctuates, especially across the thermocline and when the vehicle is at apogee. A correction, as described by Lueck and Picklo (1990) and more recently Garau et al. (2011), is applied to the conductivity and temperature sensor in the initial processing. The effectiveness of this correction depends on knowing the speed of the vehicle and, therefore, the speed of the flow of water through the conductivity sensor, which is reliant on determining a good flight model. Two models are derived: (1) from the change in pressure observed by the vehicle (glider-slope model) and (2) from the change in buoyancy (hydrodynamic model) of the vehicle (Frajka-Williams et al., 2011), which rely on good estimations of the gliders lift, drag, induced drag coefficients, volumes, glider absolute compressibility, and glider volumetric thermal expansion. The accuracy of these variables relies first on pre-deployment measurements and initial piloting procedures, and second by minimizing error in the flight model (e.g., regressing the glider-slope model with the hydrodynamic model, as implemented in the UEA-GliderToolbox [http://www.byqueste.com/toolbox.html]).

Error induced in the data by thermal lag is particularly pertinent in waters where the density is set by salinity; this is because salinity is most affected by thermal lag, with the correction resulting in a root mean square error of 4×10^{-3} g kg^{-1}. An analysis of the offset between climb (when the glider is ascending through the water column) and dive (when the glider is descending), that is, profiles which are close to each other in space, "∧" shape, and separately, dive and climb profiles during the deployment (profiles with a "∨" shape), highlights the regions where thermal lag most affects the data (Figure 3).

To constrain the error in our analysis of submesoscale fluxes, we quantify the error contribution to ML lateral density gradients by thermal lag. We compute the horizontal difference in density, averaged vertically

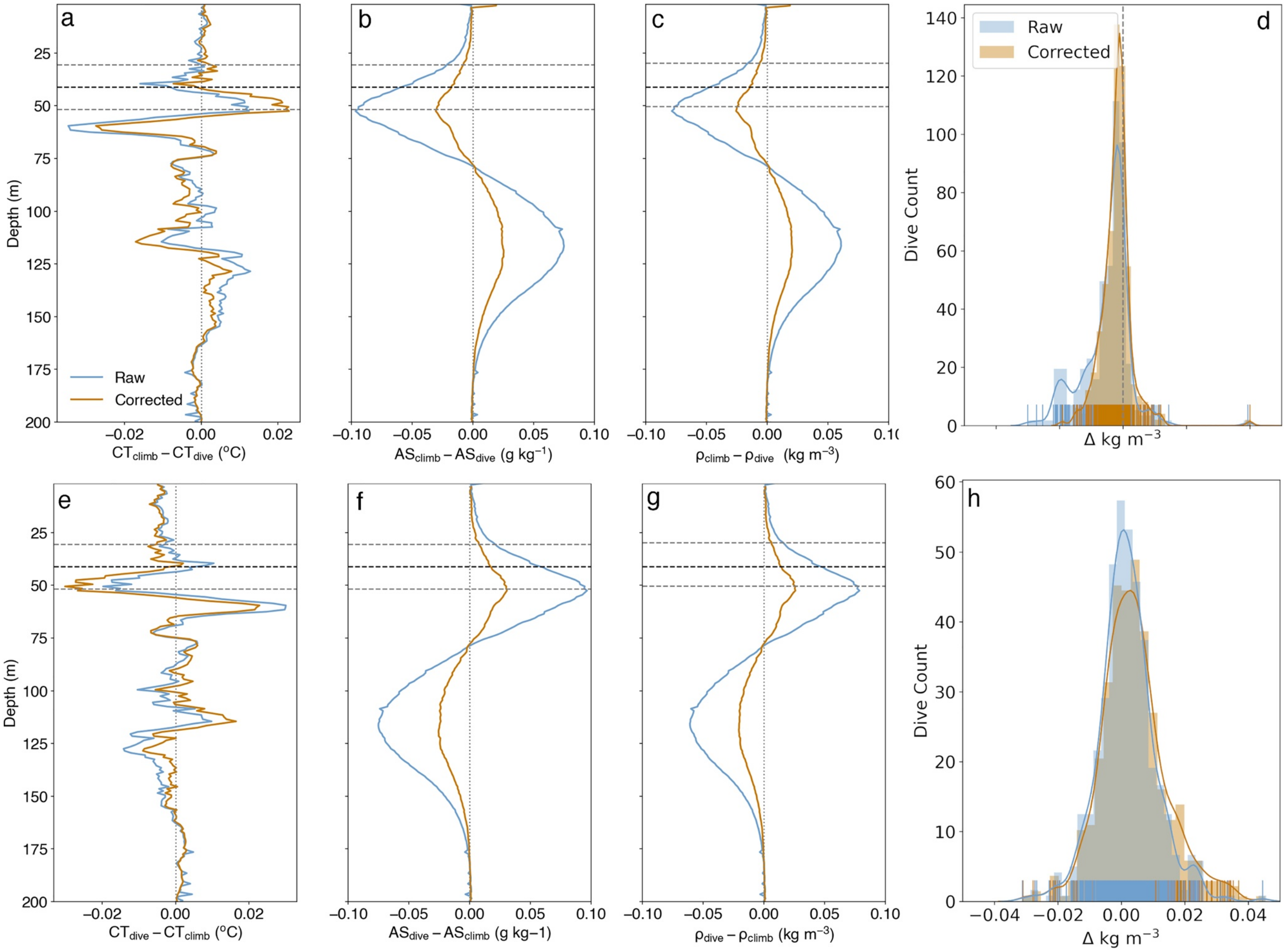

Figure 3. Seaglider uncorrected and thermal lag corrected (a and e) conservative temperature (CT), (b and f) absolute salinity (AS) and (c and g) density (ρ). The mean and standard deviation of the ML depth is indicated by dashed lines. (d and h) Distribution of the horizontal density differences, where density is vertically averaged between the surface and 15 m above the MLD, between all climb and dive Seaglider profiles. (a–c) Average of horizontal density differences between climb minus dive profiles(“∧”) (e–g) average of horizontal density differences between dive minus climb profiles (“∨”).

between the surface and 15 m above the MLD (the average MLD is 40 m), between dive-climb (climb-dive) profiles (Figures 3d and 3h). The distribution plots show a 50th percentile residual error of -1×10^{-3} kg m^{-3} in the dive-climb profiles and 0.001 kg m^{-3} in the climb-dive profiles. This skewness toward underestimating (overestimating) the density differences is consistent with the Seaglider transiting from a warmer surface layer to a cooler winter water (WW) on the dive, or from a cooler WW to a warmer surface layer on the climb.

Lateral density gradients (change in density per km) of up to 0.015 kg m^{-3} km^{-1} are captured by the Seaglider. Considering the 50th percentile residual error after correcting for thermal lag quoted above, we compute this contribution to the magnitude of lateral gradients. We estimate an overestimation of lateral density gradients per km by 6% on the climb/dive pairs and a negligible error on the dive/climb pairs (much reduced because the distance between these dive pairs is larger). The overestimation of lateral gradients due to thermal lag is likely balanced by the underestimation of these gradients caused by the Seaglider not sampling fronts perpendicularly (see Section 4.5.1).

2.4. Atmospheric Reanalysis and Satellite Data

Surface forcing was obtained from ECMWFs (European Center for Medium-Range Weather Forecasts) ERA5 reanalysis. Wind stress ($\tau = \rho_a C_D U_{10}^2$) was computed from the density of air, the drag coefficient over the ocean surface (Large & Pond, 1981) and the meridional and zonal winds at 10 m height. Net surface heat fluxes (Q_{net}) were computed from shortwave and longwave contributions, as well as latent and sensible heat fluxes. Net freshwater fluxes (FWFs) were computed as evaporation-precipitation (E-P). Sea-ice fluxes are not included because the region was sampled after the sea-ice had melted. For comparison to Q_{net}, FWF is first converted to a surface buoyancy flux and then to an equivalent heat flux with the following equation as in (Pellichero et al., 2018):

$$Q_{FWF} = \rho_0 C_p \frac{\beta}{\alpha} S_{surf} \left(E - P\right), \tag{1}$$

where $\rho_0 = 1{,}027$ kg m^{-3} is a reference density, $C_p = 4{,}000$ J K^{-1} kg^{-1} is the heat capacity of water, $\alpha = 5.7$ K^{-1} is the thermal expansion coefficient of water and $\beta = 7.8 \times 10^{-4}$ kg g^{-1}, is the haline contraction coefficient. S_{surf} is the surface salinity (taken at 15 m), and (E-P) is evaporation-precipitation.

The sea surface height fields used to determine the location of the southern boundary of the ACC are based on SSALTO/Duacs Maps of Absolute Dynamic Height (MADT), following the method of Swart et al. (2010). Daily sea-ice concentration from AMSR2 (Spreen et al., 2008), with a 6.25 km lateral resolution, was used in this study. The sea-ice sector of the Southern Ocean was defined by the winter maximum of sea-ice, with sea-ice concentration greater than 15%. The regional maps of salinity are produced from ESA's Soil Moisture Ocean Salinity (SMOS) Earth Explorer mission using de-biased sea surface salinity L3 v4 maps that were generated by LOCEAN/ACRI-ST Expertise Center (Boutin et al., 2018). The global standard deviation of SMOS is 0.20 psu in the open ocean, compared to 100-km averaged ship SSS, but in polar seas, this is increased. Acknowledging this, we use SMOS only to characterize the regional impact of sea-ice on salinity, rather than relying on the actual magnitude in salinity. The surface chlorophyll map was produced with Level 2 data from the Copernicus Sentinel-3 Ocean and Land Color Instrument.

2.5. Buoyancy Gradients

Along-track (as measured by the Seaglider) time series of buoyancy were calculated as

$$b = g(1 - \rho / \rho_o). \tag{2}$$

where g is gravity and ρ_o is as defined in Equation 1. The contribution of temperature and salinity to the magnitude of lateral (along-track) density gradients was computed as:

$$b_x = g\alpha \frac{\partial T}{\partial x} - g\beta \frac{\partial S}{\partial x}. \tag{3}$$

By design, Seagliders sample in a “saw tooth” pattern as they propel themselves through adjusting their buoyancy. This results in ML (z ∼ 10–40 m) profiles which are captured at high resolution ($x \sim 300$ m) between a climb profile and a dive profile, and profiles that are further apart ($x \sim 4$ km) between a dive profile and a climb profile. An in-depth analysis of the implications of this sampling pattern in capturing lateral gradients in the ML is provided by (Swart et al., 2020) (see Figure S2).

The calculation of lateral buoyancy gradients $\frac{\partial b}{\partial x}$ and associated submesoscale fluxes necessitated interpolation onto a uniform grid. For this analysis, along-track measurements of temperature and salinity, after binning to 1 m vertical bins, were linearly interpolated onto a uniform grid of $\partial x = 1$ km, from which density and buoyancy were computed. The ML lateral buoyancy gradient is computed as the along-track buoyancy in the middle of the ML. Errors may be introduced as a result of thermal lag (as discussed in Section 2.3) as well as through interpolating across non-uniform distances. Errors in buoyancy are expected to lead to amplified errors in buoyancy gradients when the measurements are closer together.

2.6. Stratification and Turner Angle Analysis

The Brunt-Väisälä frequency is computed and decomposed into contributions from temperature and salinity using the following formulation:

$$N_{ts}^2 = \frac{\partial b}{\partial z} = g\alpha\frac{\partial T}{\partial z} - g\beta\frac{\partial S}{\partial z}. \tag{4}$$

The relative influence of temperature and salinity on vertical density stratification (N^2) is quantified with the Turner angle, which is defined as Tu = arctan(R_p), using the density ratio $R_p \equiv \alpha\frac{\partial T}{\partial z}\left(\beta\frac{\partial S}{\partial z}\right)^{-1}$ (Turner, 1973). $\frac{\partial T}{\partial z}$ and $\frac{\partial S}{\partial z}$ are the vertical derivatives of temperature and salinity. The Turner angle is positive when temperature and salinity have competing effects on density stratification. For $Tu = \pi/4$, temperature stratification is fully compensated by salinity stratification. For $Tu = -\pi/4$, salinity and temperature contribute equally to the density stratification. Salinity stratification exceeds the contribution from temperature stratification when $-\pi/4 < Tu < \pi/4$, and temperature stratification dominates when $|Tu| > \pi/4$.

Similarly, a horizontal Turner angle can be defined by replacing the vertical gradient in temperature with a horizontal gradient. In this way the temperature and salinity contribution to lateral fronts can be decomposed. Fronts in which the Turner angle is positive are at least partially compensated, with $Tu > \pi/4$ indicating that temperature has a stronger impact on density than salinity. Fronts where $Tu < 0$ are anti-compensated in which salinity and temperature are acting constructively to create differences in density. These situations have the potential to produce strong density fronts; however, horizontal density gradients can slump due to gravity and may not persist (Rudnick & Cole, 2011). The horizontal Turner angle is computed using a length scale of 1 km.

To test whether the distribution in the vertical and horizontal Turner angles changes over the course of the summer season, the data is split into the first quartile (early summer) and last quartile (late summer) of the full data set until the atmospheric heat flux becomes zero. Each quartile consists of 500 data points, equivalent to 22 and 25 days in early and late summer, respectively, a temporal resolution of roughly 1 h.

2.7. Submesoscale Equivalent Heat Fluxes

The non-dimensional Richardson number $\left(Ri = \frac{N^2}{(\partial u \,/\, \partial z)^2} = \frac{f^2}{N^2}\left(\frac{\partial x}{\partial z}\right)^2\right)$, which provides a ratio between vertical stratification and geostrophic shear, characterizes the dynamic regime where large values, $Ri \gg 1$, represent quasi-geostrophic flow and small values, $Ri \approx 1$, an ageostrophic regime where submesoscale flows may be active. Using Seaglider observations, we apply the thermal wind assumption such that geostrophic shear is given by the squared along-track lateral gradient normalised by the Coriolis acceleration to give the bulk Richardson number, $Ri_b = \frac{f^2 N^2}{b_x^2}$.

MLIs develop through cross-frontal motion that results in the stretching or compression of fluid parcels. Because vorticity is conserved during this process, there is an inverse cascade of energy and eddies are formed (referred to as MLEs), that typically manifest at horizontal scales O (0.1–10 km) and can induce vertical velocities of O(100) m day^{-1} (Boccaletti et al., 2007) by converting horizontal buoyancy gradients into vertical gradients. This overturning of density surfaces restratifies the water column and can be expressed in terms of a vertical stream function (Fox-Kemper et al., 2008):

$$\psi_{MLI} = 0.06\frac{\mu(z) b_x H^2}{|f|}, \tag{5}$$

where μ, represents the vertical structure and is set to unity for simplicity and H is the depth of the ML. The vertical buoyancy flux associated with the MLI stream function can be represented as an equivalent heat flux (Mahadevan et al., 2012):

$$Q_{MLE} = 0.06 \frac{b_x^2 H^2}{|f|} \frac{C_p \rho_0}{\alpha g}, \tag{6}$$

where 0.06 is an empirically defined coefficient determined by numerical models (Fox-Kemper et al., 2008) and b_x is the along-track buoyancy gradient. Because the MLI parameterization by Fox-Kemper et al. (2008) is based on the assumption that MLI grow from the potential energy stored in mesoscale lateral gradients, we applied a rolling window of 8 km (~4 times the ML Rossby radius of deformation) such that the Q_{MLE} values estimated here are based on the mesoscale field.

While Q_{MLE} is always positive and acts to restratify the ML, cross-frontal Ekman-driven flow by overlying wind fields results in lateral density advection. In particular, surface wind stress oriented downfront, or in the direction of the geostrophic shear, produces an Ekman transport that advects less buoyant over more buoyant water, a condition that is gravitationally unstable and induces turbulent mixing, arresting restratification. This mechanical surface forcing can, similarly to MLI, be expressed as an equivalent heat flux, referred to as Ekman buoyancy flux (EBF), which involves the component of the wind stress aligned with the submesoscale front (D'Asaro et al., 2011; Thomas & Lee, 2005):

$$Q_{EBF} = -\frac{b_x \tau^y}{f} \frac{C_p}{\alpha g}. \tag{7}$$

In calculating the along-front (across-track) wind stress, the wind will not always be aligned with the surface fronts. Following Viglione et al. (2018), the winds were rotated relative to the Seaglider orientation to determine the wind stress component perpendicular to the Seaglider's trajectory (τ^Y). Negative values of Q_{EBF} correspond to destabilizing, down-front conditions.

For this analysis, we assume the Ekman layer is equivalent to the MLD. This assumption simplifies the vertical structure of the upper ocean. While we acknowledge this is a non-trivial assumption, the equivalence of the MLD and the Ekman layer is perhaps reasonable under these summer conditions, when the ML is shallow and the winds are strong. A scaling analysis of the Ekman depth based on a κ_d, the turbulent diffusivity, ~ 0.1 m^2 s^{-1}, gives an Ekman depth ($H_E = \sqrt{2\kappa_d / f}$) of about 40 m, which is the average MLD of the upper ocean in these observations.

A case study is presented to contextualize the results described later in this study. A subset of the Seaglider observations (with the Seaglider moving both in the southward direction and the northward direction; horizontal distance covered by glider in the case study is 30.5 km) and winds from which the submesoscale processes of MLI and EBF are computed is shown in Figure 4. EBF is positive (restratifying) under conditions where the across-track winds are oriented upfront. Upfront winds are defined when the across-track winds and along-track b_x observed by the Seaglider have the same sign. For example, during the northward transect, negative b_x and negative τ^Y indicate lighter, more buoyant water to the south in combination with westerly winds. In the southern hemisphere, westerly winds result in Ekman transport to the north, pushing lighter water over denser water and restratification.

3. Results

3.1. Mixed Layer Properties

The ML properties evolve over summer from cold and fresh (34 g kg^{-1}, −1.2°C), to warmer and saltier (1.5°C, 34.2 g kg^{-1}, Figure 5). A cold, relatively salty WW layer, defined as the temperature minimum layer below the 1,027.5 kg m^{-3} isopycnal, separates the ML from the warm and salty upper Circumpolar Deep Water (uCDW) at the 1,027.7 kg m^{-3} isopycnal (see Figure S1). Four days after the complete melt of sea-ice, the surface layer had shoaled from ~100 m (observed by a nearby SOCCOM float, see Figure S2) to 41.0 m, gradually deepening to 80 m over the 3-month glider deployment.

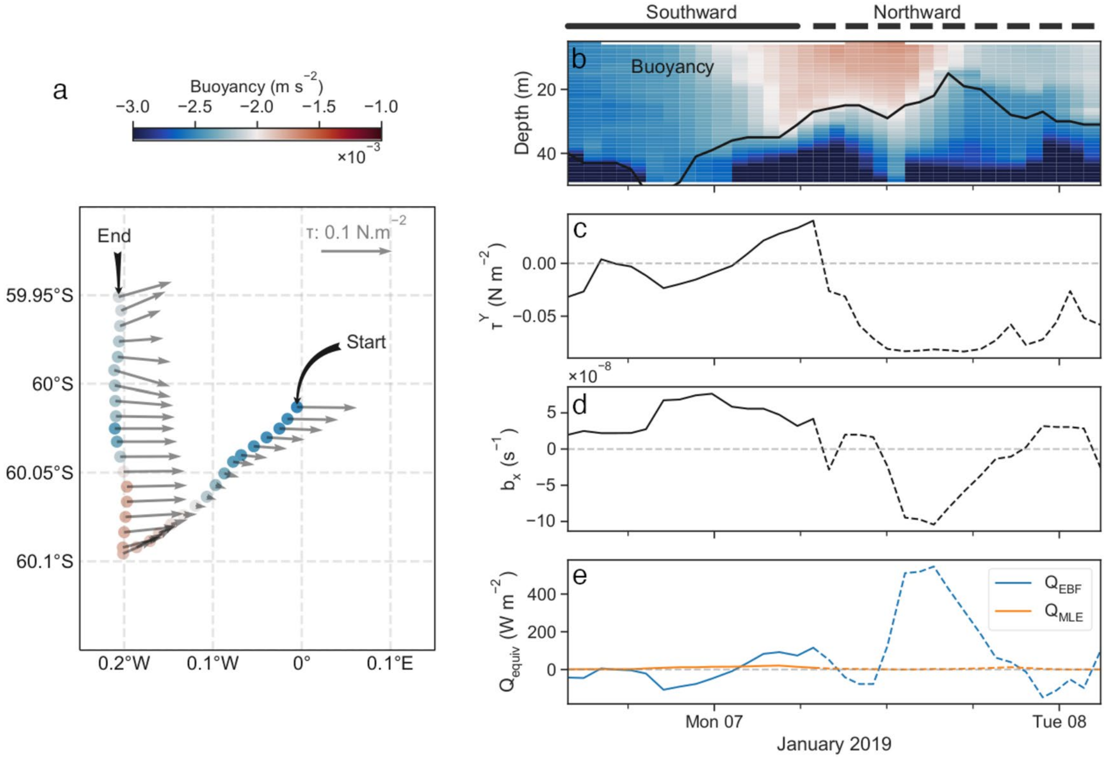

Figure 4. Case study of Seaglider observations during which a strong lateral gradient was sampled. (a) Glider trajectory, colored by the buoyancy at 15 m. Black arrows indicate the start and end of the subsample. Wind stress vectors are overlaid in gray. (b) Section of buoyancy with the mixed layer depth overlaid in black. (c) Wind stress oriented perpendicular to the Seaglider track (positive to the left of the glider orientation). (d) Along-track buoyancy gradient as observed by the Seaglider. (e) Estimated submesoscale equivalent heat fluxes (Q_{equiv}): Q_{MLE}, Q_{EBF}. The solid lines indicate when the Seaglider was moving southwards, while the dashed lines indicate when the Seaglider was moving northwards. The entire distance covered by the glider in this case study is 30.5 km.

ML buoyancy increases from -3×10^{-3} m s^{-2} in December to -1.5×10^{-3} m s^{-2} by late February, before decreasing again. Buoyancy gradients of up to 1.5×10^{-7} s^{-2} are observed, equivalent to density fronts of 0.015 kg m^{-3} km^{-1}, and salinity fronts of 0.02 g kg^{-1} km^{-1}. The largest lateral buoyancy gradients (those greater than 5×10^{-8} s^{-2}, Figure 5d) are observed until mid-February. Early summer is characterized by N^2 values at the base of the ML of $1.1 \times 10^{-4} \pm 4.6 \times 10^{-5}$ s^{-2}, which decrease in late summer to $6.7 \times 10^{-5} \pm 3.9 \times 10^{-5}$ s^{-2}. Toward the end of summer, from ∼ 8 March, the ML deepens to 80 m, WW isopycnals move closer together, and stratification at the base of the ML increases again to $1.4 \times 10^{-4} \pm 6.6 \times 10^{-5}$ s^{-1} in March.

Seaglider observed conditions in the upper ocean are embedded within a larger mesoscale field. In this region, and during the sea-ice melt season, the mesoscale field is predominantly structured by northwards advecting freshwater from sea-ice melt. The freshwater signal emanating from the melting sea-ice, observed in SMOS sea surface salinity (Figure 1a), is mirrored in the Seaglider profiles (Figure 5a) and specifically in the first mesoscale transect (Figure 6a). Low saline water is advected northwards by the predominantly westerly winds. We confirm this by estimating the Ekman component of the salinity tendency budget from lateral salinity gradients observed during the mesoscale transects.

$$\frac{\partial S_{Ekman}}{\partial t} = -U_e.\nabla S_m, \tag{8}$$

where

$$U_e = \frac{1}{\rho_o f H}\begin{pmatrix} \tau^y \\ -\tau^x \end{pmatrix} \tag{9}$$

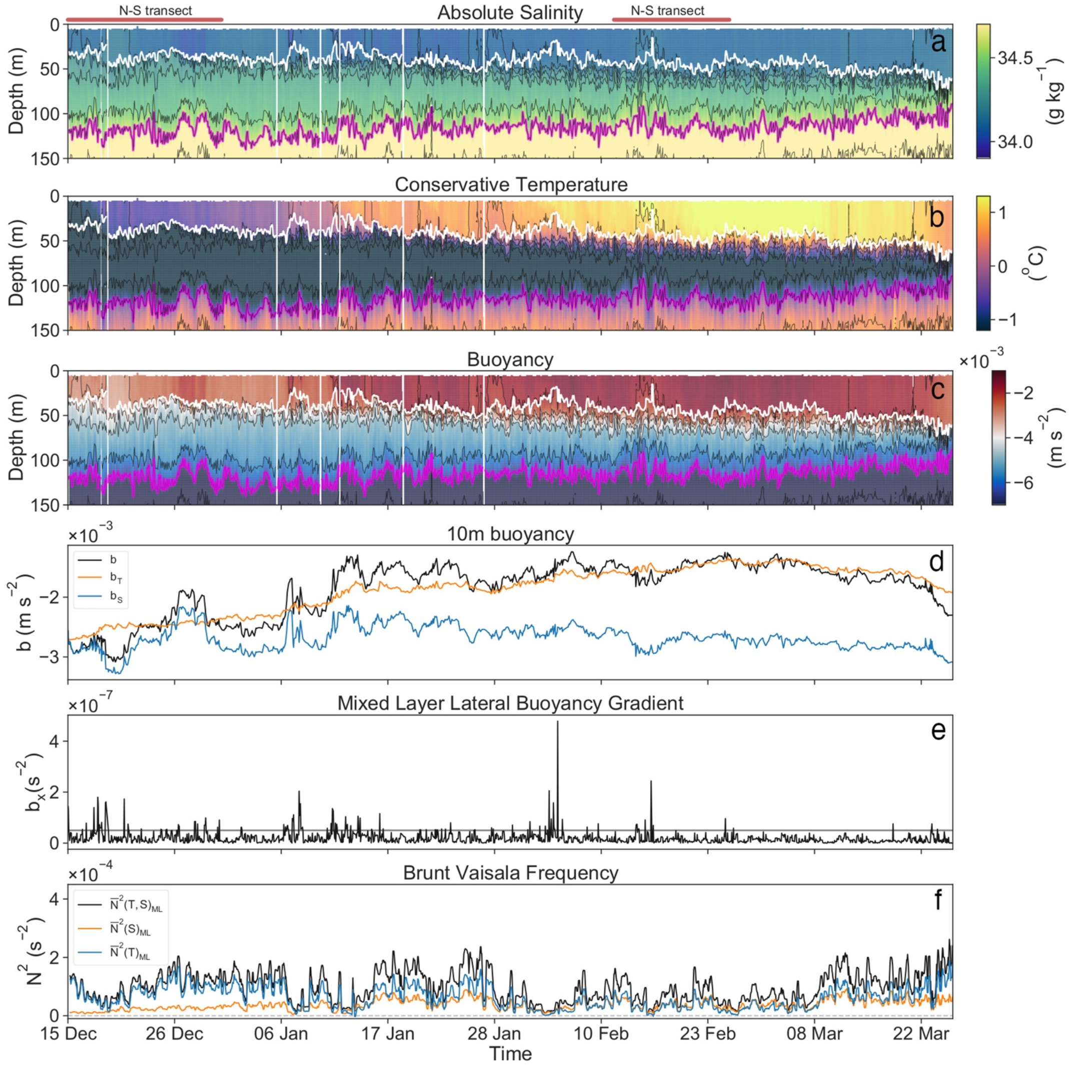

Figure 5. Time series of the summer season 2018-2019: (a) Seaglider sampled absolute salinity. Thin black lines denote density isopycnals with an interval of 0.01 kg m^{-3}. The mixed layer depth is shown in white. The lower bound of winter water is marked with magenta lines, identified by the density isopycnal = 1,027.7 kg m^{-3}, the temperature maximum beneath the mixed layer. (b) The same as (a) but for conservative temperature; (c) The same as (a) but for buoyancy. (d) Temperature and salinity contribution to ML buoyancy (at 10 m depth). (e) The average mixed layer buoyancy gradients and (f) Temperature and salinity contribution to vertical stratification at the base of the mixed layer. The solid red lines above the plot indicate when the Seaglider was completing mesoscale transects.

$\frac{\partial S_{Ekman}}{\partial t}$ is computed by taking an average across-track wind stress of 0.09 N m^{-2} to the east (note that the wind stress varies synoptically and not seasonally), and the large scale gradient across the two mesoscale transects shown in Figure 6. The Ekman contribution to the upper ocean salinity tendency is larger than or comparable to the salinity tendency attributable to FWF by evaporation and precipitation ($\frac{\partial S_{Ekman}}{\partial t} \sim 2.1 \times 10^{-8}$ g kg^{-1} s^{-1} and $\frac{\partial S_{FWF}}{\partial t} \sim 4.8 \times 10^{-9}$ g kg^{-1} s^{-1}). The contribution of S_{ekman} decreases in the second mesoscale transect as the mesoscale lateral salinity gradient decreases (Figure 6b), potentially indicating a decrease in freshwater advection northwards.

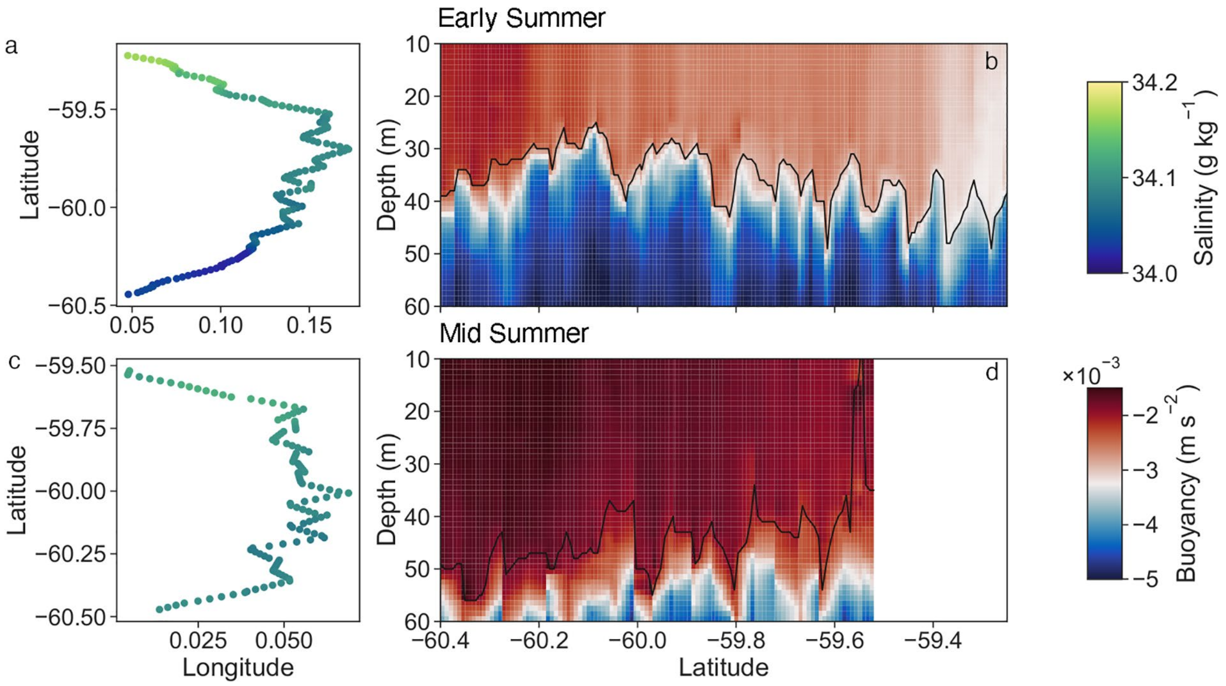

Figure 6. Subset of the Seaglider data showing the mesoscale transects at the beginning (a and b) and middle of the deployment (c and d). Panels (a and c) show the Seaglider trajectory with salinity overlaid. Panels (c and d) are sections of the glider-observed buoyancy. Black lines in (c and d) are the mixed layer depth.

3.2. Vertical and Lateral Stratification

To quantify the contribution of salinity and temperature to ML density, the vertical and horizontal Turner angles were computed. In both cases, the haline contribution to density decreases as the season progresses (Figure 7).

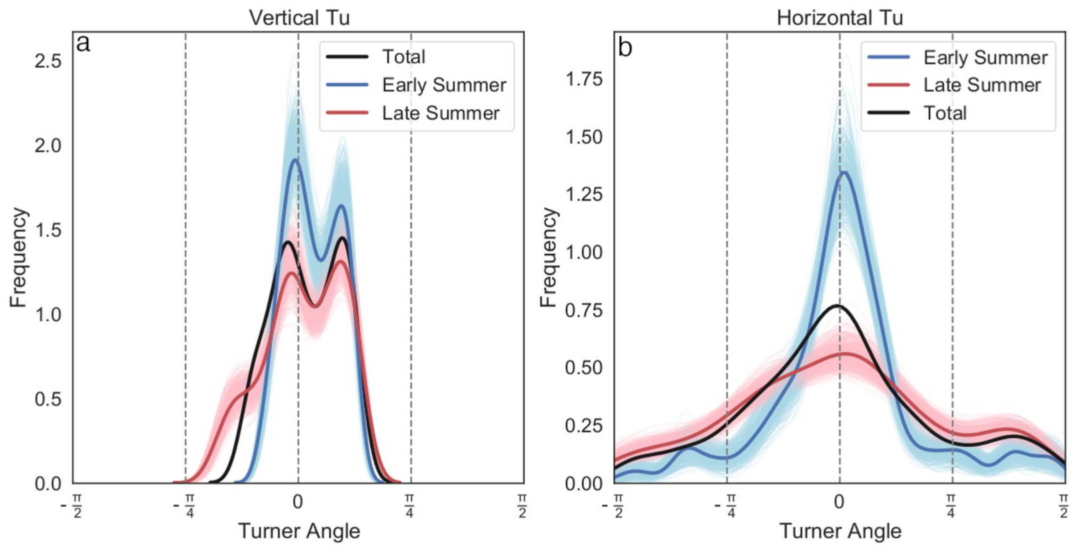

Figure 7. Distribution of the Turner angle in the upper ocean at 60°S, 0°E during summer (black line), decomposed into early summer (blue line) and late summer (red line). (a) Histogram of the vertical Turner angle averaged in the upper 200 m. (b) Histogram of the horizontal Turner angle. Bootstrapping was applied to the early summer and later summer subsets to give the confidence intervals marked in light blue and pink shading, respectively.

In the vertical, the average Turner angle of the upper 200 m reveals a bimodal structure representing the interface between the surface water and WW, and the interface between uCDW and WW (shown in the time series, Figures 5a and 5b). In late summer, the distribution of the vertical Turner angle shifts toward $\frac{-\pi}{4}$, representing the increased role of temperature in setting vertical stratification.

Similar to the vertical stratification, lateral density variations in the ML are determined by salinity anomalies during early summer (Turner angle distribution centered at zero, Figure 7b), moving toward mixed salinity and temperature compensated fronts in late summer (distribution broadens).

3.3. Submesoscale Instabilities and Fluxes

Wavenumber spectra are used to describe the horizontal density variance in the ML and analyze the seasonal timescale of active scales of energy variance. There is a growing body of literature to describe submesoscale turbulence based on the spectral slopes of energy and tracer variance, assuming constant stratification (see review by Jaeger et al., 2020). While constant stratification is rare in the world's ocean, and theoretical power laws in question are based on the assumptions of an inertial subrange and of statistical homogeneity of the flow field, the spectra nevertheless provide a useful metric with which to assess scales of variance in the ocean.

Interior quasi-geostrophic (IQG) turbulence theory, which typically scales with variance slopes of $\sim k^{-3}$ (Charney, 1971) describes turbulence that originates from deep baroclinic instabilities and is applicable away from surface boundaries because it assumes no ML and constant density at the boundary. Surface quasi-geostrophic (SQG) theory (Blumen, 1978), assumes a buoyancy gradient which, through stirring of this gradient, results in frontogenesis and a cascade of eddies to give an inertial subrange of $k^{-5/3}$. Both these scaling laws describe flows that are in geostrophic balance, and need to be adjusted for an ageostrophic component of the flow, which tends to steepen SQG energy and tracer slopes to k^{-2} (Boyd, 1992; Capet et al., 2008). Considering the assumptions behind these power laws and the errors that propagate in observations, observations have not always confirmed these predictions. Jaeger et al. (2020) review the existing observational literature of spectral analysis with a focus on tracer analysis, finding that in most cases, the power laws are inconsistent with both IQG and SQG and being more consistent with ageostrophic frontogenesis theory which predicts power laws of k^{-2}.

In this study, both meso- (~100 km) and submeso- (<10 km) scales were resolved. After separating the glider transects into these two scales (Figure 1c), the wavenumber power spectrum of density (potential energy) variance is computed for both the mesoscale (Figure 8a, $N = 2$) and submesoscale (Figures 8b and 8c, $N = 36$) glider transects in the ML (10 m). In the following analysis, we assume that density spectra are a proxy for potential energy spectra. By taking the spectra of density, we measure the variance of density at different wavenumbers. The integral over all the wavenumbers gives the total density variance, which can be converted to potential energy by dividing by N^2 and multiplying by relevant constants. Typically, N^2 is assumed to be constant, leaving density variance an appropriate measure of potential energy variance. A multi-taper method with adaptive weighting and five smoothing windows is applied. Discrete prolate spheroidal sequences (DPSSs) are used as data windowing functions. Confidence intervals are determined from a X^2distribution for which the degrees of freedom are computed as a function of the number of windowed segments and the length of the spectra. The instrument noise is determined to be 3 km and marked on the plots. Inertial subrange slopes are then computed for the mesoscale transects between 50 and 3 km and for the submesoscale transects between 8 km (the full depth Rossby radius of deformation) and 3 km.

While the mesoscale transects are more informative as they capture a larger range of scales, the submesoscale transects are additionally taken into account, the averages of which allow for the assumption of statistical stationarity. There is a trade-off with this assumption because of a level of uncertainty in the shorter transects due to the inertial subrange being computed over only one order of magnitude.

The mesoscale snapshots display spectra with inertial subrange slopes of $k^{-2.16 \pm 0.2}$ and $k^{-2.2 \pm 0.3}$ in early summer and late summer, respectively-essentially remaining constant over the season. The submesoscale

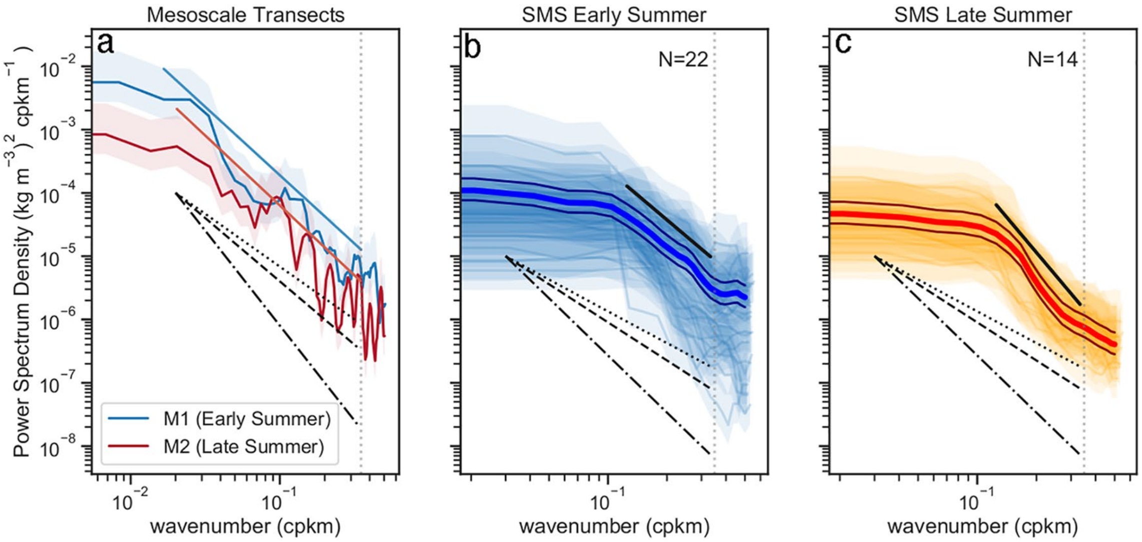

Figure 8. Power spectra of density at 10 m for (a) the glider mesoscale transects and (b) submesoscale transects during early summer (December to January, $N = 22$ transects) and (c) submesoscale transects during late summer (February to March, $N = 14$ transects). The 95% confidence interval (CI) of the spectra is shaded, the 95% CI for the average spectra is indicated by solid lines adjacent to the average spectra in (b) and (c). The noise cutoff wavenumber (3 km), is marked by the gray dotted line. Inertial subrange slopes are calculated for the mesoscale transects between 50 and 3 km. The slope in the first mesoscale transect (M1) is $k^{-2.16 \pm 0.2}$ and $k^{-2.2 \pm 0.3}$ in the later transect (M2). Inertial subrange slopes for the submesoscale transects in (b and c) are computed over the range 8–3 km to give average slopes of $k^{-2.6 \pm 0.2}$ and $k^{-3.6 \pm 0.3}$, respectively. Reference slopes of $k^{-5/3}$ (dotted line), k^{-2} (dashed line), and k^{-3} (dash-dot line) are indicated in the figure.

slopes have an average slope of $k^{-2.6 \pm 0.2}$ and $k^{-3.6 \pm 0.3}$ in early and late summer, respectively. The individual submesoscale transects are noisy, ranging from k^{-1} to k^{-4}. The total potential energy in the system (integration under the spectra, assuming constant N^2) is reduced toward late summer.

We focus our analysis on the potential for MLI to form the submesoscale structure suggested in Figure 8. Conditions where lateral gradients have scales of O(1) km and stratification is weak (Richardson numbers ~ O(1)), indicate when the water column is predisposed for submesoscale overturning to occur. We assess the wavelength and growth rate of the fastest growing MLI, defined as (Fox-Kemper et al., 2008; Stone, 1970):

$$l_{max} = \frac{2\pi U}{f}\sqrt{\frac{1+Ri}{5/2}}, \tag{10}$$

$$\tau_{max} = \sqrt{\frac{54}{5}}\,\frac{\sqrt{1+Ri}}{f}, \tag{11}$$

U, is the geostrophic velocity in the ML, determined by multiplying H by the geostrophic shear, calculated from the Seaglider derived lateral buoyancy gradient, as $|b_x|/f$, under the assumption of thermal wind balance:

$$U \equiv \frac{|\,b_x\,|}{f}H.$$

For the ice-free Antarctic MIZ during summer, taking $Ri = 1$, a typical maximum growth rate is 10 h, using $f \sim 1.26 \times 10^{-4}\ \mathrm{s}^{-1}$, the local inertial frequency, with a typical length scale of 1.4 km (using a MLD of 40 m and lateral buoyancy gradient of $1 \times 10^{-7}\ \mathrm{s}^{-1}$). These scales are comparable to simulations by Fox-Kemper et al. (2008), in which a MLD of 100 m and $b_x^2 = 2f^2$, results in $\tau_{max} \sim 16.8$ h and $l \sim 3.9$ km.

Using the Seaglider measured lateral buoyancy gradient, MLD and Richardson number, we extend the analysis of the MLI growth rate and wavelength to the full-time series (Figure 9). Within the ML, the

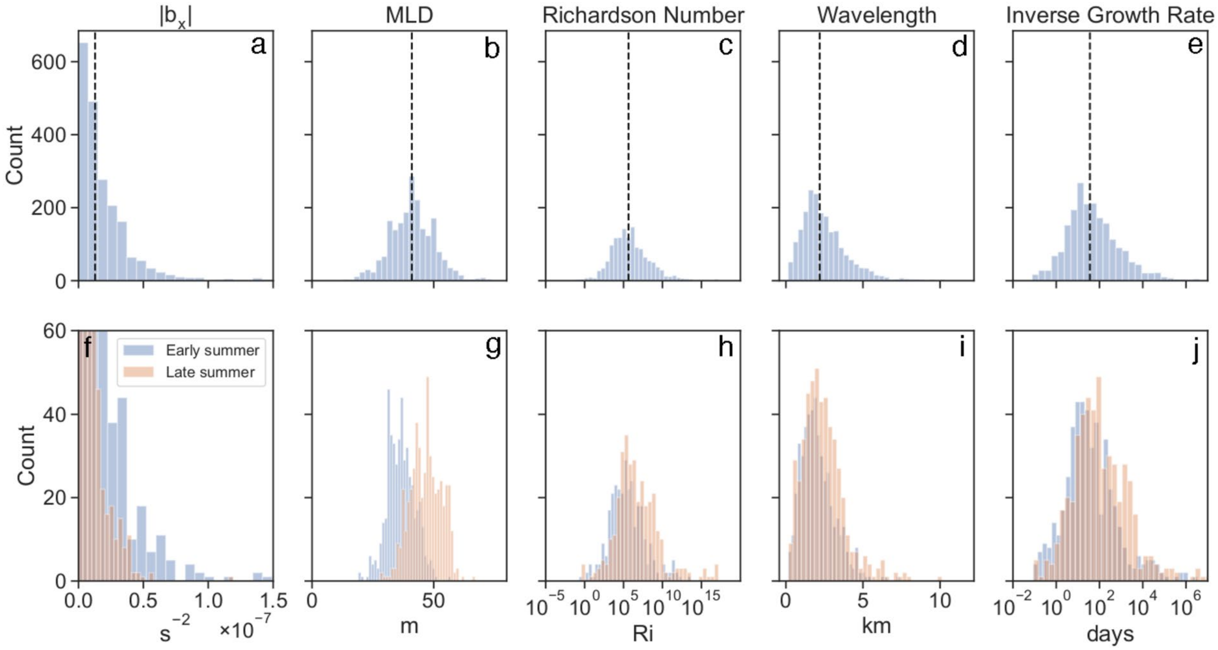

Figure 9. Histograms of: (a) magnitude of along-track buoyancy gradient, (b) MLD, (c) Richardson number, (d) MLI wavelength, (e) MLI inverse growth rate. Median values are indicated by the black dashed lines. Panels (f and j) show the seasonal shift in distributions of (a–e) from early summer to late summer using the same definitions as in Figure 5. MLD, mixed layer depth; MLI, mixed layer instability.

Richardson number varied over several orders of magnitude (Figure 9c), a function of stratification at the base of the ML and the strength of the lateral buoyancy gradients. During the summer season, most of the ML flows are characterized by Ri $\gg$ 1, influenced by the strong stratification resulting from the recent sea-ice melt, $Ri_{ML} \sim 1 \times 10^5$. Very intermittently, a combination of weaker stratification and strong lateral buoyancy gradients brings the system toward an ageostrophic regime where $Ri_{ML} < 4$ in 2% of profiles (Figure 9c). The distribution of the magnitude of lateral buoyancy gradients is skewed to the left, with the majority of lateral gradients being weak (Figure 9a). In early summer, the occurrence of strong lateral buoyancy gradients is more frequent than during later summer (Figure 9f). For the same time period, the distribution of MLD is centered around a mean value of ~ 40 m, with 98% of the observations found between 15 and 75 m (Figure 9b), shifting to a deeper average during late summer (Figure 9g). The majority of the distribution of the wavelength of the fastest growing MLI is typically less than 5 km (Figure 9d), similar to the ML Rossby radius of deformation, $Lr = \mathrm{NH}/f = 2 \pm 0.6$ km. The inverse growth rate of MLI is a function of the Richardson number and follows a similar distribution to that of the Richardson number (Figure 9e). The Richardson number, wavelength, and growth rate of MLI display a tendency toward higher magnitudes during late summer (Figures 9h and 9j). Together, these results suggest that the upper ocean undergoes a shift from early summer to late summer in the scales that describe the instabilities and eddies.

Similarly, MLE fluxes and EBF, which both depend on lateral buoyancy gradients, weaken as the summer season progresses and the strength of lateral buoyancy gradients decreases (Figure 10). When MLIs are active, their stratifying potential is weak (<50 W m^{-2}). Conversely, wind interactions with ML fronts have the potential to impact stratification in the ML, with the observed submesoscale fronts ($b_x \sim$ (O) 5×10^{-8} s^{-2}), sufficient to induce EBF fluxes greater than 200 W m^{-2}. Together, EBF and MLE increase the variability of the total equivalent heat flux in the ML during early summer by 55% (from a standard deviation of 35.9 W m^{-2} to 80.5 W m^{-2}), compared to late summer when the influence of submesoscale fluxes is almost negligible (standard deviation increases from 32.4 to 34.4 W m^{-2} with the inclusion of submesoscale fluxes) (Figure 10c).

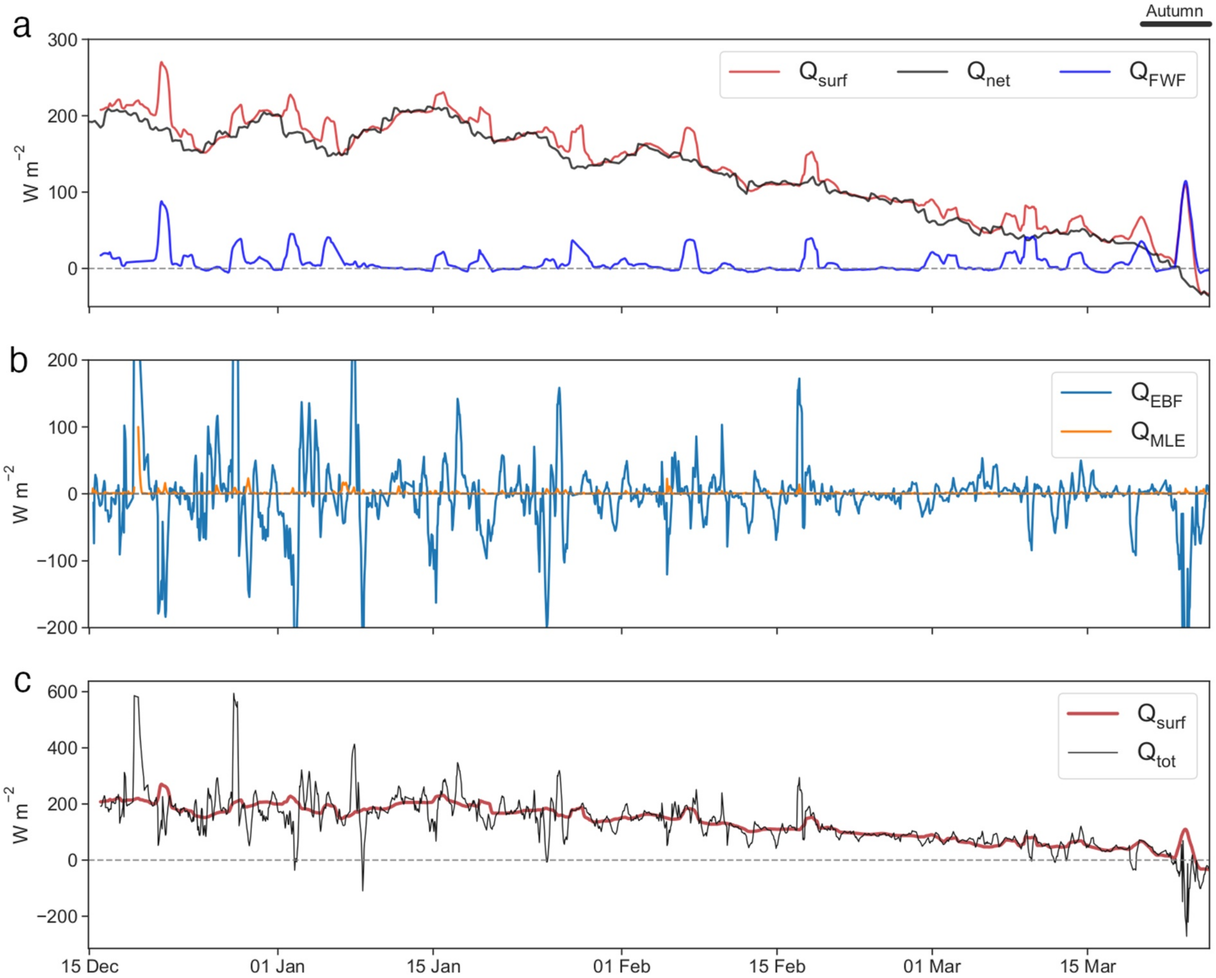

Figure 10. Timeseries of the summer season 2018–2019: (a) Surface heat flux (Q_{net}, black) and equivalent freshwater flux ($Q_{freshwater}$, blue) are expressed as an equivalent heat flux from ERA5 reanalysis and the sum of the two (Q_{surf}, red). Rolling means of 24 h are applied. (b) Equivalent heat flux by submesoscale overturning due to mixed layer baroclinic instability (Q_{MLE}, orange) and Ekman Buoyancy Flux (Q_{EBF}, blue). A rolling mean of the inertial period (10 h) was applied to Q_{EBF} to reduce the emphasis on sporadic events. (c) Sum of the total surface buoyancy forcing, restratification due to MLEs, and wind-driven submesoscale Ekman transport ($Q_{tot} = Q_{surf} + Q_{MLE} + Q_{EBF}$) expressed as an equivalent heat flux. The red curve shows Q_{surf} as in (a) for reference. The onset of autumn is indicated by the black line above the plot, defined by a shift from positive to negative heat flux into the ocean. *Note*. The change in scale on the *y*-axis.

4. Discussion

This study investigates ML dynamics over a summer season in the Antarctic MIZ, in which our three main aims are addressed. First, we investigate whether ML fronts, formed by recent sea-ice meltwater, remain prevalent during the early summer in the ice-free MIZ. Second, we characterize submesoscale flows as the summer season progresses, and third, we evaluate their impact on the structure of the ML, such as its depth and stratification.

4.1. A Salinity-Driven System

We find a shift from salinity-dominated to mixed salinity/temperature-controlled buoyancy variability through the progression of the summer season. Salinity-driven buoyancy variability is expected in the ice-impacted Southern Ocean, where sea-ice-derived waters drive the seasonal ML salinity budget (Pellichero et al., 2017). Similar occurrences are observed in the Arctic MIZ, with salinity driving ML density variability during ice-free conditions (Timmermans & Winsor, 2013).

Initially, cold, low saline water is advected through the sample region, and positive buoyancy anomalies, driven by salinity, are observed (Figure 5). ML buoyancy becomes more sensitive to temperature fluctuations as the summer season progresses, with temperature exerting a stronger influence on density. This is also reflected in the flattening of the horizontal turner angle distribution (Figure 7). In early summer, the water temperatures are cold (<1°C), and thus temperature has a small impact on buoyancy because of nonlinearities in the equation of state. As the water temperatures increase, so too does the thermal expansion coefficient and, correspondingly, the temperature contribution to buoyancy. In this region, the largest contributor to positive surface buoyancy flux is solar heating. Increased buoyancy associated with a warmer ML increases the stability of the ML, with the potential to suppress MLI.

Temperature determines the seasonal trend in ML buoyancy (Figure 5c), but variations in salinity that continue throughout the season give rise to lateral density gradients. Salinity contribution to buoyancy varies around a stationary mean, reflecting swirling horizontal gradients likely characteristic of submesoscale eddies (McWilliams, 2016), and providing evidence that MLEs may be contributing to the observed lateral buoyancy gradients.

The time series we present here extends beyond that of Swart et al. (2020), in which they show that submesoscale fronts persist into summer in an interplay between thermohaline slumping by winds and frontogenesis. Corresponding with their observations, lateral buoyancy gradients observed here persist from December to February, but eventually reduce in magnitude from mid-February until the end of March when the surface heat flux turns negative (Figure 2) and the supply of freshwater from the south decreases (Figure 6). While the strength of the overlying westerlies does not noticeably diminish, the amount of freshwater available to advect northwards decreases as the sea-ice reaches its minimum extent, ~1,000 km south of the study site (Figure 1a). The dampening of surface lateral buoyancy gradients in late summer may reflect this loss of a source of positive buoyancy anomalies. In summary, our observations support the hypothesis that sharp (e.g., $b_x > 5 \times 10^{-8}\ \mathrm{s}^{-2}$, Figure 5c) sea-ice meltwater fronts persist in the ice-impacted Southern Ocean after the sea-ice has melted.

4.2. Summer Submesoscale Processes

We observed salinity-driven lateral fronts at submesoscales during summer in the ice-free Antarctic MIZ, with increased prevalence occurring with close proximity to the sea-ice melt out (occurring at this study site on December 10, 2018, Figure 1d). This frontal structure agrees with concurrent surface observations described by Swart et al. (2020) (Figure 3, density spectral slopes scaling at $k^{-2.4}$), revealing an active submesoscale regime during early summer. The mesoscale and submesoscale density spectral slopes observed by the Seaglider in this study range from k^{-2} to steeper than k^{-3} (Figure 8). In this study, while the mesoscale slopes converge at $k^{-2.2}$ (Figure 8a); the submesoscale slopes show more variability (Figures 8b and 8c). It remains challenging to distinguish the contributions of different physical mechanisms from spectral slopes (Erickson et al., 2020). Nevertheless, below, we present potential explanations for the change in density spectra slopes from that predicted by theory.

The physical interpretation of the potential energy inertial subrange in the upper ocean is best described by SQG which predicts a slope of $k^{-5/3}$, while observations and models which include an ageostrophic component steepen the SQG predicted slope to $k^{-2.2}$. For SQG in the ML, the tracer spectra and potential energy spectra follow the same power law (Callies & Ferrari, 2013). Global observations of tracer spectral slopes are mostly steeper than $k^{-5/3}$ (Jaeger et al., 2020). In the observations presented in Figure 8, $k^{-5/3}$ and k^{-2} are not robustly distinguishable given the noise across the individual transects, and we continue the discussion with reference to k^{-2}. IQG, which predicts steeper slopes of k^{-3}, represents the energy cascade in the interior ocean and is thus not applicable for the surface ocean. In the literature, the steeper density slopes have been interpreted to describe an upper ocean in which eddy kinetic energy is small; therefore, the majority of the energy is injected at larger mesoscales with a tendency for an inverse cascade of energy (e.g., in the Arctic and in the North Pacific; Callies & Ferrari, 2013; Timmermans et al., 2012; Timmermans & Winsor, 2013). The mesoscale slopes presented in Figure 8a present an energy cascade for this region which follows a power law steeper than predicted by SQG but not as steep as that predicted by IQG.

We hypothesize that submesoscale fronts in this region are formed from stirring of MLEs, which grow from ML instabilities. These submesoscale instabilities themselves draw energy from the larger scale mesoscale fronts that potentially stir freshwater anomalies by sea-ice melt (see Swart et al., 2020). The large inter-transect slope variability (in Figures 8b and 8c, ranging from $\sim k^{-1}$ to k^{-4}) may reflect the intermittent nature of surface turbulent motion in the region. That this variability decreases over the summer season and the slope steepens (Figure 8c), is suggestive that the tight interplay between strong stratifying forcing and turbulent motion decreases later in summer, to give way to a generally quiescent ocean. As the summer season progresses and the sea-ice meltwater fronts are mixed and/or advected out of the region, the available potential energy for MLIs decreases (the magnitude of the integration of the density spectra decreases, which is directly related to APE through the QG approximation of constant N^2, Figure 8a). At the same time, the frequency of strong submesoscale fronts in this region decreases toward the late summer (Figure 5e).

While there is a possibility that the steeper slopes observed in the later part of the summer season in Figure 8c are revealing a more quiescent ocean at the submesoscale, this is not reflected in the mesoscale transect (M2, Figure 8a), and it is acknowledged that there is a large amount of uncertainty in the data and methods to robustly come to this conclusion.

Uncertainties may arise from the high sensitivity of the slope to the wavenumber band chosen as well as the range over which the slope is calculated, with increased uncertainty when computed over a single order of magnitude (as in the submesoscale transects presented). A further source of error may be linked to the glider being unable to capture all the energy at large wavenumbers (small-scale structure) and artificially steepening the spectral slopes (the glider horizontal sampling resolution is limited to ∼300 m to 3 km). In the latter half of the observations, the slope steepens to $k^{-3.6}$. With a weaker background gradient, it is possible that the glider observations are not high resolution enough to capture the fine-scale energy during this time and so the slope appears steeper. Further errors may be introduced into these spectra as a result of the necessary linear interpolation (Callies & Ferrari, 2013; Klymak et al., 2015).

Even though a submesoscale regime is evident (Figure 10), we found that if the fine-scale fronts observed reflect stirring of MLEs, their impact on surface stratification is weak (Q_{MLE} = 5–20 W m^{-2}). With an average surface heat flux of 200 W m^{-2}, restratification by MLEs is not large enough to compete. Winds oriented up or down front have impacts on the lifetime of the fronts with implications to mixing and the persistence of fronts. EBF varies between 100 and 1,000 W m^{-2}, up to two orders of magnitude greater than Q_{MLE}, and often larger than the ambient surface heat flux. EBF acts to intermittently increase stratification or increase mixing. The effect of winds interacting with ML fronts, decreases later in summer. These results indicate that mechanical wind-forced interactions with the observed fine-scale fronts can be important to the ML structure. Estimates of MLI and EBF are slightly larger than that estimated by Swart et al. (2020) for the same region during summer ($Q_{MLE} \sim$ O(10) W m^{-2}, $Q_{EBF} \sim$ O(100) W m^{-2}), likely linked to their data record only beginning during late summer conditions and the higher resolution of our sampling (0.3–4 km vs. ∼ 9 km in Biddle & Swart, 2020).

North of the southern boundary of the ACC, similar submesoscale fluxes have been observed in the regions between the ACC jets. EKE is relatively weak and MLD is <100 m resulting in similar MLE fluxes to this study (du Plessis et al., 2019), but in the energetic Drake Passage, MLs are deeper (MLD > 100 m) and lateral gradients are stronger (up to 3×10^{-7} s^{-2}), providing MLE fluxes that can reach up to 4,000 W m^{-2} (Viglione et al., 2018). By definition, MLEs draw more APE from deeper MLDs (Fox-Kemper et al., 2008). The potential for MLE fluxes in our data is thus limited by the relatively shallow summer MLDs. A secondary peak in MLE potential during early autumn in the Antarctic MIZ, concurrent with ML deepening, is shown by Biddle and Swart (2020). Similarly, at the end of this data set, with the onset of autumn and a deepening ML, MLEs begin to increase in magnitude again.

An alternative mechanism, that accounts for the large MLI wavelength and growth rates predicted by linear instability theory (Figure 9), and perhaps contributes to the steepening of the spectral slopes (Figure 8) is that the small scale lateral buoyancy gradients are evidence that there is a tendency for weak frontogenesis in the upper ocean due to the strong lateral density gradient imposed by sea-ice melt. The seasonal decrease in the total magnitude of density variability in the upper ocean (Figure 8), together with the small (∼2 km) ML Rossby radius of deformation, allows for balanced fronts and filaments that have been drawn out by mesoscale stirring to persist at small-scales in this region. These surface anomalies would have a signature in the power spectra at the submesoscale, but not generate mixed-layer eddies or increased vertical velocities. Nevertheless, these weak fronts would likely be surface confined due to the strong stratification imposed by sea-ice meltwater.

In the Southern Ocean, denser waters are generally located to the south, with lighter waters to the north. The predominantly westerly winds over this meridional gradient in density create a large-scale destratifying EBF over the region. Within the ACC, similar observations of EBF to the present study support this mechanism at the submesoscale as well (du Plessis et al., 2019). Conversely, at the MIZ, after sea-ice melt, the meridional gradient is variable as lighter fresher water advects northwards intermittently, resulting in both stratifying and destratifying EBF under similar wind forcing (Figures 10 and S3).

These results show that while submesoscale front generation is likely due to mesoscale stirring of freshwater, stratification may be more strongly influenced by wind-front interactions, represented here by EBF. These findings are in line with previous observations in the Weddell Sea (Biddle & Swart, 2020), suggesting that these dynamics are not limited to the year of this study.

4.3. Mixed Layer Response to Submesoscale Flow

It is challenging to infer the impact of submesoscale flow on the ML structure empirically due to the ephemeral nature of submesoscales together with the multiple processes that impact the variability of the MLD. Yet, our summer data provides evidence that submesoscale processes actively modify the ML, but likely do not penetrate below the ML.

The sea-ice impacted ML reflects the influence of atmosphere-ocean fluxes, sea-ice, and internal ocean variability. Here, we have focused on the relative contribution and interactions of atmospheric forcing, sea-ice, and submesoscale flows to the ML structure. Heat flux into the ocean is the dominant process in setting the ML stratification over the summer season, with a relatively small contribution from evaporation and precipitation (Figure 10a). Nevertheless, ML buoyancy anomalies are driven by salinity changes, even well into the summer season (although the magnitude of the anomalies decreases).

In our study, MLEs have weak stratifying potential over the summer season (Figure 10b). Under summer conditions, when the ML is shallow, there is less available potential energy for MLEs to restratify the upper ocean. Nevertheless, model studies (Callies & Ferrari, 2018) show that MLIs are unlikely to be damped out in shallow summer MLs, even if mixing time scales are short. One possibility is that MLIs do grow and lead to restratification of the ML in summer after sea-ice melt but quickly exhaust the energy fueling their growth.

The significant contribution of EBF to the upper ocean surface equivalent heat flux was observed, particularly in early summer following sea-ice melt (Figure 10). In some studies, submesoscale activity under shallow ML conditions has resulted in deepening MLs (Luo et al., 2016; Lévy et al., 2010) due to the increased vertical mixing induced by the fronts that erode the shallow base of the ML. In this study, while we do not test the evolution of the ML structure with and without the inclusion of submesoscale activity, we speculate that the Antarctic MIZ could be responding similarly and observe a gradual deepening of the ML over the summer season. The presence of fine-scale fronts as a result of swirling MLEs may enhance upper ocean mixing through interactions with surface wind stress. Evidence that this may be the case is presented at the end of the observational time series (~ March 20, 2018, Figure 10). A strong wind and precipitation event (Figures 3b and 3c) occur over a strong lateral buoyancy gradient ($>1 \times 10^{-7}$ s^{-2}), inducing very strong submesoscale EBF (>500 W m^{-2}), with the potential to erode the base of the ML and mix the underlying waters into the ML. Similar strength wind events occurred before in the time series (January 18, 2018 and ~ March 10, 2018), but during those times, the lateral buoyancy gradients were weak, and thus EBF was not significant. Because of the intermittency of both the passing wind events and the submesoscale MLEs, it is probable that similar events were missed by the observational platform. It could be speculated, that in nearby regions unobserved by the Seaglider, these wind events, in combination with the lateral buoyancy gradients, may be driving local mixing more than if the submesoscale flows were not active (i.e., when the upper ocean is more homogeneous, winds may not have a large impact).

Here, we argue that the fine-scale lateral gradients observed are representative of MLEs. Mesoscale eddies are present in the region, as evidenced by surface chlorophyll-a (map in Figure 1); however, these are likely concentrated further north near the Southern Boundary of the ACC. If mesoscale stirring is important for frontogenesis (Manucharyan & Thompson, 2017), these fronts, similar to those associated with MLEs in the region, would not penetrate deep into the water column, as sea-ice melt maintains strong vertical stratification. This emphasizes two points: (1) that most of the buoyancy anomalies observed in the ML were confined to the ML, and (2) the confinement of surface fronts in the ML suggests that there is a limited exchange with the interior as a result of sea-ice melt that increases upper ocean stratification and prevents strong cross-isopycnal transport.

Combined, these results support the hypothesis that sea-ice melt enhances the generation of surface fronts. These fronts can potentially allow for large EBF, which impacts the ML structure during early summer in the Antarctic MIZ. In particular, our evidence highlights the role of submesoscale wind-front interactions to maintain weaker early summer stratification at the base of the ML under otherwise highly stratifying conditions in a relatively quiescent ocean.

4.4. Implications

As per Swart et al. (2020), we have shown that submesoscale flow is more active during early summer after sea-ice has melted, most likely energized by the regional impact of meltwater fronts, than later in the summer season. Meltwater is an important driver of water mass transformation in the Southern Ocean (Abernathey et al., 2016; Pellichero et al., 2018). In the summer, the shallow ML of the ice-impacted Southern Ocean is subject to transformation through the influx of fresher meltwater, solar heating, stirring by both mesoscale and submesoscale flows, and the passage of strong wind events. We find that MLI has a low potential to restratify the ML and subduct water to depth. This confirms the necessary advection of these modified waters northward, or potentially downstream in the ACC, before subducting as Antarctic intermediate water (AAIW) and connecting with the global circulation system (e.g., Figure 1; Pellichero et al., 2018). The substantial increase in the impact of winds on the ML when strong lateral buoyancy gradients or fronts are present, provides a secondary mechanism for eroding the base of the ML and mixing with the underlying warmer and saltier waters. It is interesting to consider whether wind interactions with submesoscale flow play an important role in mixing the uCDW waters into the ML. uCDW waters are warm, salty, and high in nutrients; thus, the upwards mixing of these waters will act to support primary production as well as modify the properties of the ML. The implications for ML interior exchange in this region under weak MLEs but stronger EBF when submesoscale fronts are active or reduced is an avenue for future research.

Current models and observations indicate that the Southern Ocean is freshening (Haumann et al., 2016, 2020). Even though the ML may become shallower as it becomes fresher, it is likely that MLI will persist (Callies & Ferrari, 2018), and the dynamics described here will continue to be relevant. It has been suggested that the predicted shallower MLs of a warming climate will suppress submesoscale activity (Richards et al., 2020). Here, we show an Antarctic example with evidence of submesoscale activity when the ML is shallow.

4.5. Caveats

4.5.1. Frontal Processes Observed by Gliders

ML lateral buoyancy gradients are a central parameter in much of the analysis presented in this study. The interpretation of ML fronts observed by profiling gliders is not trivial, and a number of assumptions were made in the presentation of the results.

In this field campaign, the Seaglider was piloted to complete repeat bow-tie patterns over a single geographical area. A complete bow-tie took, on average, 7 days to complete. Sampling fronts in this way means that the Seaglider may sample a single front multiple times. Given the transient nature of surface submesoscale fronts and an ML eddy growth rate of ∼10 h, it is unlikely that the same front is indeed sampled multiple times by the Seaglider. Moreover, the background mean flow was ∼8 cm s^{-1}, compared to the velocity of the Seaglider ∼23 cm s^{-1}. Nevertheless, the data is analyzed such that the results do not rely on repeat sampling of a front, or the sampling of many fronts, but provides a basis by which to statistically estimate the average presence and strength of these fine-scale fronts and associated impact on the ML, acknowledging that individual features can be very different.

We assume the Seaglider samples fronts perpendicularly. Acknowledging this is not the case, a statistical analysis shows that the lateral gradients are underestimated by a factor of 0.64. Compared to the lateral gradients captured by a Sailbuoy (measuring values of b_x up to 0.06 kg m^{-3} km^{-1}, Swart et al., 2020), which was sampling the study site concurrently, the lateral gradients observed by the Seaglider are small (b_x up to 0.015 kg m^{-3} km^{-1}), but nevertheless comparable to those observed in the Arctic MIZ by Seagliders (∼ 0.03 kg m^{-3} km^{-1}, Timmermans & Winsor, 2013).

Additionally, synoptic winds are not always oriented directly downstream or upstream of the fronts. The Seaglider interpretation of the EBF can be analyzed by computing the observed EBF (EBF_{obs}) to the actual EBF (EBF_{actual}), estimated from all the observed Seaglider angles and wind angles with respect to a fixed buoyancy gradient (following Thompson et al., 2016). The Seaglider tends to capture either all or little of the EBF; however, this method can also overestimate EBF under conditions where the glider perpendicularly crosses the lateral buoyancy gradient while the wind is aligned perpendicular to the front, when, our definition would interpret the wind as aligned parallel to the front and thus overestimate EBF. On average, the ratio of the root mean square of EBF_{obs} to EBF_{actual} is 0.71, suggesting that the EBF values presented here are underestimated.

4.5.2. Regionality

We present the results with reference to Antarctic MIZs, but our conclusions are drawn from a subset of high-resolution data within a $1° \times 1°$ degree box at the northern edge of the Weddell Sea MIZ. We focus on the interactions of processes that are likely prevalent throughout the ice-impacted Southern Ocean. However, we acknowledge that the Antarctic MIZ varies regionally in terms of atmospheric forcing. For example, the Amundsen Sea Low (ASL) controls winds near West Antarctica. If the zonal winds are intensified because of a deeper ASL, the melt of sea-ice occurs earlier in the spring season and solar warming over summer is enhanced (Holland et al., 2017). In such a case, it is likely that submesoscale processes will be more suppressed during summer. In this way, different regions may experience different leading order forcing mechanisms (like the ASL), which may alter the conclusions drawn from these results.

5. Conclusion

Throughout this study, we have demonstrated the influence of sea-ice-derived freshwater on the vertical and lateral structure of the ML. Predominantly northwards, Ekman transport of sea-ice meltwater stratifies the ML in the Antarctic MIZ. However, at the same time, the strong north-south mesoscale gradients that stir early summer sea-ice meltwater create conditions for the formation of fine-scale fronts. We show that while these fronts are confined to the surface boundary layer because of the strong stratification, wind interactions with the resultant fine-scale fronts enhance ML variability and thus the rate of upper ocean modification. The winds interact with the fine-scale fronts, increasing variability within the ML through both stratifying and destratifying buoyancy fluxes induced by cross-front Ekman-driven transport. When the freshwater source decreases later in summer, the magnitude of lateral buoyancy gradients, as well as the submesoscale EBF also decrease. These results show that sea-ice impacted MLs, while predominantly forced by the 1D influx of meltwater during summer, cannot be solely treated as 1D systems. Submesoscale fronts are enhanced by the meltwater mesoscale gradients, modulating the influence of winds on the ML. It, therefore, becomes possible that the ML response to wind forcing and, subsequently, heat and freshwater transport, may be misrepresented in coupled-climate models if the submesoscale is not resolved or accurately parameterized.

Data Availability Statement

ERA5 data are generated using Copernicus Climate Change Service Information, available online (www.ecmwf.int/en/forecasts/datasets/archive-datasets/reanalysis-datasets/era5). All the data used for this analysis can be accessed online (ftp://ssh.roammiz.com) via anonymous login and navigate to giddy_2020. The code used to produce this analysis is available at http://doi.org/10.5281/zenodo.4043036.

Acknowledgments

This work was supported by the following grants of S. Swart: Wallenberg Academy Fellowship (WAF 2015.0186), Swedish Research Council (VR 2019-04400), STINT-NRF Mobility Grant (STNT180910357293). S. A. Nicholson and S. Swart: NRF-SANAP (SNA170522231782, SANAP200324510487) and S. A. Nicholson, the Young Researchers Establishment Fund (YREF 2019 0000007361). S. Swart and M. du Plessis have received funding from the European Union's Horizon 2020 research and innovation program under Grant agreement no. 821001 (SO-CHIC). A. F. Thompson is supported by ONR (N00014-19-1-2421), NSF (1756956, 1829969), and a Linde Center Discovery Fund grant. The authors thank Sea Technology Services (STS), SANAP, the captain, and crew of the S.A. Agulhas II for their fieldwork/technical assistance. Zach Erickson, Mar Flexas, and Giuliana Viglione (Caltech) contributed to glider piloting throughout the deployment. S. Swart is grateful to Geoff Shilling and Craig Lee (APL, University of Washington) for hosting gliders on IOP. B. Queste is thanked for insightful discussions on glider processing and thermal lag corrections, which was made possible through the UCT-UEA Newton Fund. Special thanks is extended to Isabelle Ansorge for the generous support of I. Giddy in her doctoral studies and training, from which this paper is derived (SANAP 110733 SAMOC-SA). I. Giddy is further supported by the Oppenheimer Memorial Trust. The authors are grateful to the insightful and constructive reviews of Dr. Balwada and one anonymous reviewer, which greatly improved this manuscript.

References

Abernathey, R. P., Cerovecki, I., Holland, P. R., Newsom, E., Mazloff, M., & Talley, L. D. (2016). Water-mass transformation by sea ice in the upper branch of the Southern Ocean overturning. *Nature Geoscience*, *9*(8), 596–601. https://doi.org/10.1038/ngeo2749

Biddle, L. C., & Swart, S. (2020). The observed seasonal cycle of submesoscale processes in the Antarctic marginal ice zone. *Journal of Geophysical Research: Oceans*, *125*(6). https://doi.org/10.1029/2019JC015587

Bitz, C. M., Gent, P. R., Woodgate, R. A., Holland, M. M., & Lindsay, R. (2006). The influence of sea ice on ocean heat uptake in response to increasing CO_2. *Journal of Climate*, *19*(11), 2437–2450. https://doi.org/10.1175/JCLI3756.1

Blumen, W. (1978). Uniform potential vorticity flow: Part I. Theory of wave interactions and two-dimensional turbulence. *Journal of the Atmospheric Sciences*, *35*(5), 774–783. https://doi.org/10.1175/1520-0469(1978)035⟨0774:UPVFPI⟩2.0.CO;2

Boccaletti, G., Ferrari, R., & Fox-Kemper, B. (2007). Mixed layer instabilities and restratification. *Journal of Physical Oceanography*, *37*(9), 2228–2250. https://doi.org/10.1175/JPO3101.1

Boutin, J., Vergely, J. L., Marchand, S., D'Amico, F., Hasson, A., Kolodziejczyk, N., & Vialard, J. (2018). New SMOS sea surface salinity with reduced systematic errors and improved variability. *Remote Sensing of Environment*, *214*, 115–134. https://doi.org/10.1016/j.rse.2018.05.022

Boyd, J. P. (1992). The energy spectrum of fronts: Time evolution of shocks in Burgers equation. *Journal of the Atmospheric Sciences*, *49*(2), 128–139. https://doi.org/10.1175/1520-0469(1992)049⟨0128:TESOFT⟩2.0.CO;2

Brenner, S., Rainville, L., Thomson, J., & Lee, C. (2020). The evolution of a shallow front in the Arctic marginal ice zone. *Elementa: Science of the Anthropocene*, *8*(1), 17. https://doi.org/10.1525/elementa.413

Callies, J., & Ferrari, R. (2013). Interpreting energy and tracer spectra of upper-ocean turbulence in the submesoscale range (1200 km). *Journal of Physical Oceanography*, *43*(11), 2456–2474. https://doi.org/10.1175/JPO-D-13-063.1

Callies, J., & Ferrari, R. (2018). Baroclinic instability in the presence of convection. *Journal of Physical Oceanography*, *48*(1), 45–60. https://doi.org/10.1175/JPO-D-17-0028.1

Callies, J., Ferrari, R., Klymak, J. M., & Gula, J. (2015). Seasonality in submesoscale turbulence. *Nature Communications*, *6*(1), 6862. https://doi.org/10.1038/ncomms7862

Capet, X., McWilliams, J. C., Molemaker, M. J., & Shchepetkin, A. F. (2008). Mesoscale to submesoscale transition in the California current system. Part II: Frontal processes. *Journal of Physical Oceanography*, *38*(1), 44–64. https://doi.org/10.1175/2007JPO3672.1

Charney, J. G. (1971). Geostrophic turbulence. *Journal of the Atmospheric Sciences*, *28*(6), 1087–1095. https://doi.org/10.1175/1520-0469(1971)028⟨1087:GT⟩2.0.CO;2

Chemke, R., & Polvani, L. M. (2020). Using multiple large ensembles to elucidate the discrepancy between the 1979–2019 modeled and observed Antarctic sea ice trends. *Geophysical Research Letters*. *47*(15), e2020GL088339. https://doi.org/10.1029/2020GL088339

D'Asaro, E., Lee, C., Rainville, L., Harcourt, R., & Thomas, L. (2011). Enhanced turbulence and energy dissipation at ocean fronts. *Science*, *332*(6027), 318. https://doi.org/10.1126/science.1201515

de Boyer Montgut, C., Madec, G., Fischer, A. S., Lazar, A., & Iudicone, D. (2004). Mixed layer depth over the global ocean: An examination of profile data and a profile-based climatology. *Journal of Geophysical Research*, *109*(C12). https://doi.org/10.1029/2004JC002378

Dewey, S. R., Morison, J. H., & Zhang, J. (2017). An edge-referenced surface fresh layer in the Beaufort Sea seasonal ice zone. *Journal of Physical Oceanography*, *47*(5), 1125–1144. https://doi.org/10.1175/JPO-D-16-0158.1

du Plessis, M., Swart, S., Ansorge, I. J., Mahadevan, A., & Thompson, A. F. (2019). Southern ocean seasonal restratification delayed by submesoscale wind–front interactions. *Journal of Physical Oceanography*, *49*(4), 1035–1053. https://doi.org/10.1175/JPO-D-18-0136.1

Erickson, Z. K., Thompson, A. F., Callies, J., Yu, X., Garabato, A. N., & Klein, P. (2020). The vertical structure of open-ocean submesoscale variability during a full seasonal cycle. *Journal of Physical Oceanography*, *50*(1), 145–160. https://doi.org/10.1175/JPO-D-19-0030.1

Fox-Kemper, B., Ferrari, R., & Hallberg, R. (2008). Parameterization of mixed layer eddies. Part I: Theory and diagnosis. *Journal of Physical Oceanography*, *38*(6), 1145–1165. https://doi.org/10.1175/2007JPO3792.1

Frajka-Williams, E., Eriksen, C. C., Rhines, P. B., & Harcourt, R. R. (2011). Determining vertical water velocities from seaglider. *Journal of Atmospheric and Oceanic Technology*, *28*(12), 1641–1656. https://doi.org/10.1175/2011JTECHO830.1

Frölicher, T., Sarmiento, J., Paynter, D., Dunne, J., Krasting, J., & Winton, M. (2015). Dominance of the Southern Ocean in anthropogenic carbon and heat uptake in CMIP5 models. *Journal of Climate*, *28*, 862–886. https://doi.org/10.1175/JCLI-D-14-00117.1

Garau, B., Ruiz, S., Zhang, W. G., Pascual, A., Heslop, E., Kerfoot, J., & Tintor, J. (2011). Thermal lag correction on Slocum CTD glider data. *Journal of Atmospheric and Oceanic Technology*, *28*(9), 1065–1071. https://doi.org/10.1175/JTECH-D-10-05030.1

Gregor, L., Ryan-Keogh, T. J., Nicholson, S.-A., du Plessis, M., Giddy, I., & Swart, S. (2019). GliderTools: A Python toolbox for processing underwater glider data. *Frontiers in Marine Science*, *6*, 738. https://doi.org/10.3389/fmars.2019.00738

Haumann, F. A., Gruber, N., & Mnnich, M. (2020). Sea-ice induced Southern Ocean subsurface warming and surface cooling in a warming climate. *AGU Advances*, *1*(2). https://doi.org/10.1029/2019AV000132

Haumann, F. A., Gruber, N., Mnnich, M., Frenger, I., & Kern, S. (2016). Sea-ice transport driving Southern Ocean salinity and its recent trends. *Nature*, *537*(7618), 89–92. https://doi.org/10.1038/nature19101

Holland, M. M., Landrum, L., Raphael, M., & Stammerjohn, S. (2017). Springtime winds drive Ross Sea ice variability and change in the following autumn. *Nature Communications*, *8*(1), 731. https://doi.org/10.1038/s41467-017-00820-0

Horvat, C., Tziperman, E., & Campin, J.-M. (2016). Interaction of sea ice floe size, ocean eddies, and sea ice melting. *Geophysical Research Letters*, *43*(15), 8083–8090. https://doi.org/10.1002/2016GL069742

Jaeger, G. S., MacKinnon, J. A., Lucas, A. J., Shroyer, E., Nash, J., Tandon, A., & Mahadevan, A. (2020). How spice is stirred in the Bay of Bengal. *Journal of Physical Oceanography*, *50*(9), 2669–2688. https://doi.org/10.1175/JPO-D-19-0077.1

Kirkman, C. H., & Bitz, C. M. (2011). The effect of the sea ice freshwater flux on Southern Ocean temperatures in CCSM3: Deep-ocean warming and delayed surface warming. *Journal of Climate*, *24*(9), 2224–2237. https://doi.org/10.1175/2010JCLI3625.1

Klymak, J. M., Crawford, W., Alford, M. H., MacKinnon, J. A., & Pinkel, R. (2015). Along-isopycnal variability of spice in the North Pacific. *Journal of Geophysical Research: Oceans*, *120*(3), 2287–2307. https://doi.org/10.1002/2013JC009421

Koenig, Z., Fer, I., Kols, E., Fossum, T. O., Norgren, P., & Ludvigsen, M. (2020). Observations of turbulence at a near surface temperature front in the Arctic Ocean. *Journal of Geophysical Research: Oceans*, *125*(4). https://doi.org/10.1029/2019JC015526

Large, W. G., & Pond, S. (1981). Open ocean momentum flux measurements in moderate to strong winds. *Journal of Physical Oceanography*, *11*(3), 324–336. https://doi.org/10.1175/1520-0485(1981)011⟨0324:OOMFMI⟩2.0.CO;2

Lévy, M., Klein, P., Tréguier, A.-M., Iovino, D., Madec, G., Masson, S., & Takahashi, K. (2010). Modifications of gyre circulation by sub-mesoscale physics. *Ocean Modelling*, *34*(1–2), 1–15. https://doi.org/10.1016/j.ocemod.2010.04.001

Lu, K., Weingartner, T., Danielson, S., Winsor, P., Dobbins, E., Martini, K., & Statscewich, H. (2015). Lateral mixing across ice meltwater fronts of the Chukchi Sea shelf. *Geophysical Research Letters*, *42*(16), 6754–6761. https://doi.org/10.1002/2015GL064967

Lueck, R. G., & Picklo, J. J. (1990). Thermal inertia of conductivity cells: Observations with a sea-bird cell. *Journal of Atmospheric and Oceanic Technology*, *7*(5), 756–768. https://doi.org/10.1175/1520-0426(1990)007⟨0756:TIOCCO⟩2.0.CO;2

Luo, H., Bracco, A., Cardona, Y., & McWilliams, J. C. (2016). Submesoscale circulation in the northern Gulf of Mexico: Surface processes and the impact of the freshwater river input. *Ocean Modelling*, *101*, 68–82. https://doi.org/10.1016/j.ocemod.2016.03.003

Mahadevan, A., D'Asaro, E., Lee, C., & Perry, M. J. (2012). Eddy-driven stratification initiates North Atlantic spring phytoplankton blooms. *Science*, *337*(6090), 54–58. https://doi.org/10.1126/science.1218740

Manucharyan, G. E., & Thompson, A. F. (2017). Submesoscale sea ice-ocean interactions in marginal ice zones. *Journal of Geophysical Research: Oceans*, *122*(12), 9455–9475. https://doi.org/10.1002/2017JC012895

McDougall, T. J., & Barker, P. M. (2011). *Getting started with TEOS-10 and the Gibbs seawater (GSW) oceanographic toolbox*. (pp. 28).

McWilliams, J. C. (2016). Submesoscale currents in the ocean. *Proceedings of the Royal Society A: Mathematical, Physical & Engineering Sciences*, *472*(2189), 20160117. https://doi.org/10.1098/rspa.2016.0117

Newman, L., Heil, P., Trebilco, R., Katsumata, K., Constable, A., van Wijk, E., & Spreen, G. (2019). Delivering sustained, coordinated, and integrated observations of the Southern Ocean for global impact. *Frontiers in Marine Science*, *6*, 433. https://doi.org/10.3389/fmars.2019.00433

Parkinson, C. L. (2014). Global sea ice coverage from satellite data: Annual cycle and 35-Yr trends. *Journal of Climate*, *27*(24), 9377–9382. https://doi.org/10.1175/JCLI-D-14-00605.1

Patoux, J., Yuan, X., & Li, C. (2009). Satellite-based midlatitude cyclone statistics over the Southern Ocean: 1. Scatterometer-derived pressure fields and storm tracking. *Journal of Geophysical Research*, *114*(D4). https://doi.org/10.1029/2008JD010873

Pellichero, V., Salle, J.-B., Chapman, C. C., & Downes, S. M. (2018). The southern ocean meridional overturning in the sea-ice sector is driven by freshwater fluxes. *Nature Communications*, *9*(1), 1789. https://doi.org/10.1038/s41467-018-04101-2

Pellichero, V., Salle, J.-B., Schmidtko, S., Roquet, F., & Charrassin, J.-B. (2017). The ocean mixed layer under Southern Ocean sea-ice: Seasonal cycle and forcing. *Journal of Geophysical Research: Oceans*, *122*(2), 1608–1633. https://doi.org/10.1002/2016JC011970

Richards, K. J., Whitt, D. B., Brett, G., Bryan, F. O., Feloy, K., & Long, M. C. (2020). The impact of climate change on ocean submesoscale activity. *Oceanography*. https://doi.org/10.1002/essoar.10503524.1

Rudnick, D. L., & Cole, S. T. (2011). On sampling the ocean using underwater gliders. *Journal of Geophysical Research*, *116*(C8). https://doi.org/10.1029/2010JC006849

Smith, M., Stammerjohn, S., Persson, O., Rainville, L., Liu, G., Perrie, W., & Thomson, J. (2018). Episodic reversal of autumn ice advance caused by release of ocean heat in the Beaufort Sea. *Journal of Geophysical Research: Oceans*, *123*(5), 3164–3185. https://doi.org/10.1002/2018JC013764

Speer, K., Rintoul, S. R., & Sloyan, B. (2000). The diabatic Deacon cell. *Journal of Physical Oceanography*, *30*(12), 3212–3222. https://doi.org/10.1175/1520-0485(2000)030⟨3212:TDDC⟩2.0.CO;2

Spreen, G., Kaleschke, L., & Heygster, G. (2008). Sea ice remote sensing using AMSR-E 89-GHz channels. *Journal of Geophysical Research*, *113*. https://doi.org/10.1029/2005JC003384

Stone, P. H. (1970). On non-geostrophic baroclinic stability: Part II. *Journal of the Atmospheric Sciences*, *27*(5), 721–726. https://doi.org/10.1175/1520-0469(1970)027⟨0721:ONGBSP⟩2.0.CO;2

Swart, S., du Plessis, M. D., Thompson, A. F., Biddle, L. C., Giddy, I., Linders, T., & Nicholson, S.-A. (2020). Submesoscale fronts in the Antarctic marginal ice zone and their response to wind forcing. *Geophysical Research Letters*, *47*(6), e2019GL086649. https://doi.org/10.1029/2019GL086649

Swart, S., Gille, S. T., Delille, B., Josey, S., Mazloff, M., Newman, L., & Zappa, C. J. (2019). Constraining Southern Ocean air-sea-ice fluxes through enhanced observations. *Frontiers in Marine Science*, *6*, 421. https://doi.org/10.3389/fmars.2019.00421

Swart, S., Speich, S., Ansorge, I. J., & Lutjeharms, J. R. E. (2010). An altimetry-based gravest empirical mode south of Africa: 1. Development and validation. *Journal of Geophysical Research*, *115*(C3), C03002. https://doi.org/10.1029/2009JC005299

Swart, S., Thomalla, S. J., & Monteiro, P. M. S. (2015). The seasonal cycle of mixed layer dynamics and phytoplankton biomass in the Sub-Antarctic Zone: A high-resolution glider experiment. *Journal of Marine Systems*, *147*, 103–115. https://doi.org/10.1016/j.jmarsys.2014.06.002

Thomas, L. N., & Lee, C. M. (2005). Intensification of ocean fronts by down-front winds. *Journal of Physical Oceanography*, *35*(6), 1086–1102. https://doi.org/10.1175/JPO2737.1

Thomas, L. N., Tandon, A., & Mahadevan, A. (2008). Submesoscale processes and dynamics. In M. W. Hecht & H. Hasumi (Eds.), *Ocean modeling in an eddying regime*. https://doi.org/10.1029/177GM04

Thompson, A. F., Lazar, A., Buckingham, C., Naveira Garabato, A. C., Damerell, G. M., & Heywood, K. J. (2016). Open-ocean submesoscale motions: A full seasonal cycle of mixed layer instabilities from gliders. *Journal of Physical Oceanography*, *46*(4), 1285–1307. https://doi.org/10.1175/JPO-D-15-0170.1

Timmermans, M.-L., Cole, S., & Toole, J. (2012). Horizontal density structure and restratification of the Arctic Ocean surface layer. *Journal of Physical Oceanography*, *42*(4), 659–668. https://doi.org/10.1175/JPO-D-11-0125.1

Timmermans, M.-L., & Winsor, P. (2013). Scales of horizontal density structure in the Chukchi Sea surface layer. *Continental Shelf Research*, *52*, 39–45. https://doi.org/10.1016/j.csr.2012.10.015

Turner, J. (1973). *Buoyancy effects in fluids*. (pp. 367). Cambridge, UK: Cambridge University Press.

Vichi, M., Eayrs, C., Alberello, A., Bekker, A., Bennetts, L., Holland, D., & Toffoli, A. (2019). Effects of an explosive polar cyclone crossing the Antarctic marginal ice zone. *Geophysical Research Letters*, *46*(11), 5948–5958. https://doi.org/10.1029/2019GL082457

Viglione, G. A., Thompson, A. F., Flexas, M. M., Sprintall, J., & Swart, S. (2018). Abrupt transitions in submesoscale structure in Southern Drake Passage: Glider observations and model results. *Journal of Physical Oceanography*, *48*(9), 2011–2027. https://doi.org/10.1175/JPO-D-17-0192.1

von Appen, W.-J., Wekerle, C., Hehemann, L., Schourup-Kristensen, V., Konrad, C., & Iversen, M. H. (2018). Observations of a submesoscale cyclonic filament in the marginal ice zone. *Geophysical Research Letters*, *45*(12), 6141–6149. https://doi.org/10.1029/2018GL077897